



Influence of Global Operating Parameters on the Reactivity of Soot Particles from Direct Injection Gasoline Engines

S. Koch¹ · F. P. Hagen^{2,3} · L. Büttner¹ · J. Hartmann¹ · A. Velji¹ · H. Kubach¹ · T. Koch¹ · H. Bockhorn² · D. Trimis² · R. Suntz³

Received: 21 December 2021 / Revised: 25 March 2022 / Accepted: 18 April 2022 / Published online: 11 May 2022
© The Author(s) 2022

Abstract

The aim of this study is to investigate the impact of global operating parameters, e.g., engine speed, brake mean effective pressure, and air–fuel ratio, of a turbocharged 4-cylinder GDI engine on the reactivity of soot particles against oxidation. The knowledge of soot reactivity is crucial for optimizing gasoline particulate filter regeneration strategies and is, consequently, a key parameter for reducing fuel consumption and CO₂ emissions. In this work, time-resolved in-cylinder soot concentrations and exhaust particle size distributions are measured by using two-color pyrometry, engine exhaust particle sizer and smoke meter, respectively. Reactivity against oxidation by molecular oxygen is determined by temperature programmed oxidation analysis. To derive a physicochemical explanation for varying soot reactivity, the morphological and nanostructural primary particle structure of collected samples is analyzed using high-resolution electron microscopy and image analysis algorithms. The results reveal that engine operating parameters affect soot reactivity differently. While engine speed has only a slight effect, a reduction of air/fuel ratio ($\lambda < 1.0$) or an increase of *BMEP* > 10 bar significantly reduces the soot oxidation reactivity. These findings give evidence, that the quality of the fuel/air mixture is a significant parameter influencing soot reactivity. Measured soot concentrations substantiate the hypothesis that low-sooty homogeneous premixed combustion of a homogeneous fuel/air mixture favors formation of high-reactive soot particle fractions. Reactive soot particle aggregates are composed of multiple soot fractions of different reactivity. Reactive primary particles are composed of short graphene-like layers and vice versa, providing a physicochemical explanation for varying soot reactivity depending on engine operating conditions.

Keywords Soot oxidation · Soot reactivity · Gasoline particulate filter · Particle properties · Carbon nanostructure

Abbreviations

BTDC	Before top dead center
DI	Direct injection
ECU	Engine control unit
BMEP	Brake mean effective pressure
EEPS	Engine exhaust particle sizer
ECU	Engine control unit
EMS	Exhaust gas measurement system

FSN	Filter smoke number
GDI	Gasoline direct injection
GPF	Gasoline particulate filter
HRTEM	High resolution transmission electron microscopy
IMEP	Indicated mean effective pressure
PM	Particulate matter
PN	Particulate number
PSS	Particulate sampling system
SM	Smoke meter
SOI	Start of injection
T _{max}	Temperature at maximum oxidation rate
TPO	Temperature programmed oxidation
TWC	Three way catalyst
UHC	Unburned hydrocarbons
VOC	Volatile organic compound

✉ S. Koch
sergej.koch@kit.edu

¹ Karlsruhe Institute of Technology, Institute of Internal Combustion Engines, Karlsruhe, Germany

² Karlsruhe Institute of Technology, Engler-Bunte-Institute, Combustion Technology, Karlsruhe, Germany

³ Karlsruhe Institute of Technology, Institute of Chemical Technology and Polymer Chemistry, Karlsruhe, Germany

1 Introduction

Modern gasoline direct injection (GDI) engines enable outstanding driving performance with moderate fuel consumption and low pollutant emissions at low unit costs. The worldwide increasing percentage of GDI engines in conventional and especially in hybrid systems underscores the benefit of this type of engines. However, the advantages of direct fuel injection (DI) with respect to the in-cylinder combustion process and efficiency are offset by the disadvantage of higher particulate emissions due to unsatisfactory mixture homogenization [1]. Combustion-generated carbonaceous particles are suspected to cause serious long-term health effects, e.g., respiratory diseases, heart attacks, or even strokes [2]. Therefore, future emission legislation foreseeably introduces stringent limits on permissible particulate emissions in terms of soot particle mass and particle number. This tendency poses major challenges for the development of gasoline engines [3].

Soot particles are formed in fuel rich zones inside the cylinders of the engine [4]. In direct fuel injection engines, soot formation is a consequence of insufficient mixture homogenization [5]. By using advanced laser-based diagnostics, Velji et al. [6] revealed that pool fires are the main cause of soot formation in the homogeneous mode of GDI engines with central injector position. However, in the stratified mode, there are both, local fuel-rich regions and pool fires that favor soot formation. Dageförde et al. [7] demonstrated that mixture homogeneity in the gas phase and fuel impingement are mainly determined by the spray penetration depth, injection strategy, tip sooting, fuel properties, and internal cylinder flow. These findings have also been confirmed by Sharma et al. [8], Potenza et al. [9], and Jiang et al. [10]. Moreover, an increased oxygen concentration in combination with an increased gas temperature in the cylinder and in the exhaust gas has a decisive influence on particle post-oxidation. Soot particle emission due to these processes can be controlled within certain limits through optimization of the in-cylinder combustion via engine operating parameters.

However, to meet future emission standards optimization of the internal combustion process by means of the operating conditions, e.g., injection strategy, is not sufficient. An important contribution to reducing particulate emissions of GDI engines is the use of gasoline particulate filters (GPFs) in exhaust gas aftertreatment systems. This profitable technology is also associated with problems in its application. Depending on the filter media structure, aging of the GPF, amount of soot deposited on the filter, flow conditions, and especially the amount of ash, GPFs trap particulate matter with a filtration efficiency of up to 99 % [11]. However, the buildup of soot layers within GPF channels leads to high backpressures causing combustion instabilities and higher

fuel consumption. Therefore, the GPF must be regenerated, i.e., the deposited soot particles must be oxidized with residual oxygen at high exhaust gas temperatures, before the maximum allowed back pressure is reached.

The time necessary for regeneration of GPFs is determined by the reactivity of soot particles against oxidation. High reactivity of soot enables comparatively low exhaust gas temperatures and short regeneration times, whereas low reactivity requires higher exhaust gas temperatures and long regeneration times. High reactivity, therefore, leads to lower active filter regeneration time, lower fuel consumption, and CO₂ emissions during the active regeneration process and consequently longer durability of the GPF unit. Therefore, the knowledge of soot oxidation behavior and particle properties determining their reactivity against oxidation at exhaust gas temperatures is of preeminent importance for optimizing GPF regeneration with respect to engine performance and additional fuel consumption. Increasing soot reactivity by adding metal-based fuel additives is of only limited use due to higher ash input into the GPF and additional components such as tank and dosing units [12]. If soot particle properties that determine their reactivity can be controlled via engine operating conditions, a versatile toolbox for optimizing GPF regeneration could be provided.

Despite common features of GDIs and DI-diesel engines regarding direct fuel injection systems, there are major differences with respect to fuel properties, mixing of air and fuel, stoichiometry, fuel injection timing, ignition strategy, and flame and exhaust gas temperatures. Therefore, it is not surprising, that particle properties such as primary particle sizes and size distributions, micro- and nanostructural particle properties, and other physical-chemical characteristic differ considerably [13–18]. From this, differences in reactivity of soot from GDIs and DI-diesel engines are expected. As emphasized in detail in [13] and [19], oxidation kinetics of soot particles can be primarily attributed to nanostructural particle characteristics. Carbon nanostructure reflects the collocation of layered graphene-like structures within the primary soot particles – referred to as fringes – distinguished by their length, curvature, and separation distance as well as defects within the crystallite structure [20]. These properties all affect the number density of accessible sites for oxidation. The more extended the graphene-like structures, the lower their ratio of outward-facing carbon atoms available by oxidation to the inward-facing C-atoms bonded within the graphene skeleton. In addition, defective fringe structures are easily functionalized by surface groups due to the lack of coordinating neighbors [21], resulting in highly reactive C-sites that are prone to oxidation at lower temperatures [20].

Besides the nanostructure of primary soot particles, the influences of primary particle size, aggregate diameter, and radius of gyration, specific surface area, oxygen functional

groups, and catalytic ash particles on reactivity are discussed in the literature. Small primary particle sizes were found to correlate with high reactivity [22] and large specific surface area has been observed to cause high reactivity [23]. The specific surface area and the pore structure of soot particles are closely connected with oxidant diffusion into the soot particles. However, reactivity of soot particles is determined by the number density of accessible active sites rather than the overall surface area [24]. Furthermore, salts, minerals, or ashes may enhance the reactivity of soot due to catalytic effects [25]. As reported in the literature, particles generated by diesel engines exhibit relatively uniform primary particle sizes and crystalline carbon nanostructure with ordered and extended graphene layers [16, 26, 27], which in turn results in low reactivity [28, 29]. In contrast to this, primary soot particles of GDI engines operated at stoichiometric conditions and homogeneous mode reveal a wide size range and are composed of more or less ordered and amorphous structures [14, 15, 30]. These smallest and highly reactive nanoparticles often show an amorphous nanostructure with short and disordered graphene-like layers without completed graphitization and a high content of internal defects [15, 19].

Seong et al. [14] found a correlation between fuel injection timing and soot nanostructure in GDI engines, suggesting that mixture formation in GDI engines has a greater impact on the nanostructure of soot particles than in diesel engines. In a recent study, the reactivity of soot particles from GDI engines at different injection strategies has been investigated [30]. The results of this work reveal that the reactivity against oxidation significantly depends on mixture homogenization which can be controlled by means of optimal adjusted injection parameters. Soot particles formed in mixtures with a high degree of homogenization due to optimized injection parameters show a high soot reactivity and vice versa. Highly reactive soot particles exhibited amorphous nanostructures with short and disordered graphene-like layers whereas less reactive soot particles contained larger, well-ordered ones. These findings are consistent with results from Miyashita et al. [31] on the effects of engine parameters on morphology of particulates emitted from GDI engines. In contrast to the referred studies, Choi et al. [32] stated that the catalytic action of ash particles is one of the driving factors enhancing reactivity against oxidation of engine generated soot. According to this study, the nanostructure of soot particles from GDI engines appears to be independent of engine parameters. This investigation, however, was conducted under non-stationary engine operating condition, e.g., cold starts, and high levels of PM emissions due to fuel impingement and, therefore, possible combustion of oil. In contrast Rinkenburger et al. found that increasing amounts of ash and inorganic particles cause a significant change

of the primary particle nanostructure during oxidation, resulting in shorter graphene-like layers and amorphous structures leading consequently to higher reactivity [25].

Summing up, the impact of the global GDI engine operation parameters on soot particle nanostructure and, therefore, on the reactivity against oxidation at exhaust gas temperatures is controversially discussed in the literature. However, the knowledge of the impact of engine operation parameters, which are most easy to tune, on reactivity is of central concern for the design of efficient GPF regeneration strategies. Therefore, in this study, morphological and nanostructural properties of soot particles collected from the exhaust gas of a GDI engine and the resulting reactivity against oxidation in dependence on global engine operation parameters, i.e., engine speed, torque, and relative air/fuel ratio, are investigated. For this, exhaust gas composition, primary particle and aggregate size distributions are determined varying the abovementioned global engine operating parameters. In addition, the nanostructural particle properties are evaluated by high-resolution transmission electron microscopy (HRTEM). Finally, soot reactivity measured via temperature programmed oxidation (TPO) is correlated with the determined particle properties at varying engine parameters. Additionally, thermodynamic parameters and soot concentrations inside the cylinder determined by two-color pyrometry are used to characterize the particle formation history. The aim of the investigation is to assess the particle properties primarily influencing reactivity of soot against oxidation at exhaust gas temperatures (300 to 600 °C) and their dependence on global engine operating parameters.

2 Experimental Setup and Methodology

In the following sections, a brief description of the test bench setup and the analytical methods used to characterize soot particle properties is given.

2.1 Engine and Test Bench Specifications

The investigation has been performed on a gasoline turbocharged 4-cylinder engine with direct fuel injection and optical access. The arrangement allows the analysis of the formation and oxidation of soot particles inside the cylinder and measurements of gaseous and particulate components in the exhaust gas. Technical key data of the engine under investigation are summarized in Table 1.

A schematic drawing of the experimental setup is given in Fig. 1. To vary the global engine parameters and operating conditions, the ETK interface to the open engine control unit (ECU) is accessed with the ETAS

Table 1 Specifications of the 4-cylinder TSI engine

Displacement	1984 cm ³
Compression ratio	10.5:1
Injector	Swirl injector, side mounted, direct injection
Test fuel	Super Plus (RON=98)
Exhaust aftertreatment system	TWC+GPF

hardware and the INCA software enabling reproducible test runs. To avoid cross influences from oil input on mixture formation and the combustion process, the experiments have been performed with an external crankcase ventilation system and fresh engine oil. As test fuel, a commercial gasoline fuel (Super Plus) has been used and all experiments were carried out with a chemically identical batch. In addition, a cylinder pressure indicating system is used to characterize the internal combustion.

2.2 Investigated Engine Operating Parameters

This study addresses the impact of engine speed, torque (brake mean effective pressure, *BMEP*), and relative air/fuel ratio λ on reactivity of GDI engine generated soot

against oxidation at low temperatures. The relative air/fuel ratio λ is defined as air/fuel ratio normalized with the air/fuel ratio at stoichiometric conditions. Table 2 provides an overview over the studied parameters, covering almost the entire global operating range of the GDI engine.

The morphological and nanostructural particle properties and the resulting reactivity of the emitted soot against oxidation have been determined at the listed variations of engine speed, torque, and relative air/fuel ratio. The knowledge of the influence of these parameters on reactivity against oxidation at exhaust gas temperatures is central for the application of effective and fuel efficient GPF regeneration strategies.

2.3 Probing Particle Number, Size Distributions, and Soot Samples

Figure 2 summarizes with the help of a simplified flow chart the general methodology and the analytical techniques used in this study. Engine operating parameters are varied as given in Table 2 (No. 1 in Fig. 2). Soot formation and oxidation inside the cylinder are monitored with the help of the two-color pyrometry as described in Sect. 2.4 (No. 2 in Fig. 2). Soot particles were collected from the exhaust gas by using a partial flow dilution

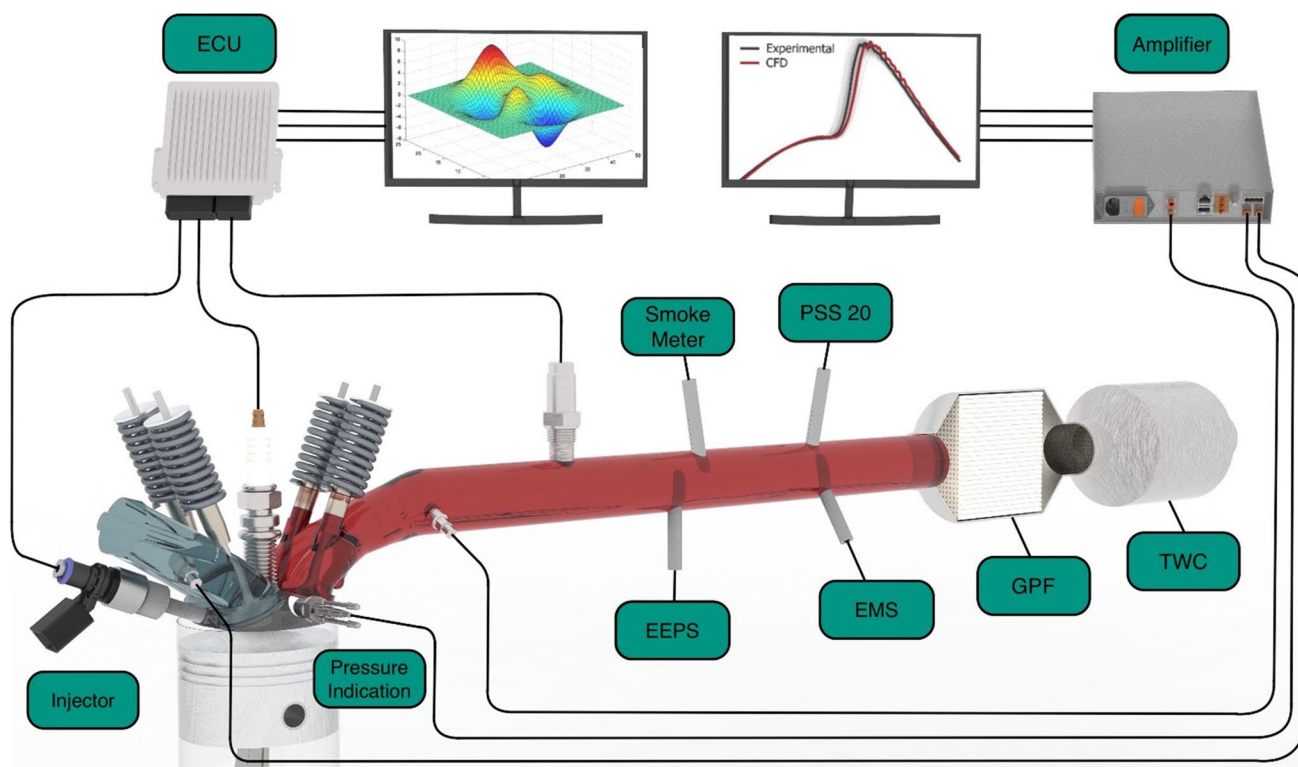


Fig. 1 Test bench specifications and overview of measuring systems (see list of abbreviations)

Table 2 Overview of investigated engine operating parameters

Variation	n [rpm]	$BMEP$ [bar]	λ [-]	SOI [° CA BTDC]	P_{Rail} [bar]	Ignition [° CA BTDC]	Camshaft overlap [° CA]
Engine speed n	1750–2750	9 (IMEP)	1	310	100	25	0
Engine load $BMEP$	2000	2–12	1	310	100	Variable	0
Relative fuel/air ratio λ	2000	8	0.7–1.2	310	100	25	0

system (particulate sampling system, PSS-20). The dilution ratio is set to 1:5. Preliminary examinations verified that the gas dilution has no impact on the soot reactivity. Particle sampling in the exhaust is performed in front of the GPF and three-way catalyst (TWC). Quartz fiber

filters are used, to separate the soot particles from the gas phase (No. 3 in Fig. 2). The loaded filters are analyzed by two ex-situ analytical methods (No. 4 in Fig. 2). While the particle morphology and nanostructure are investigated via HRTEM, the reactivity against oxidation has

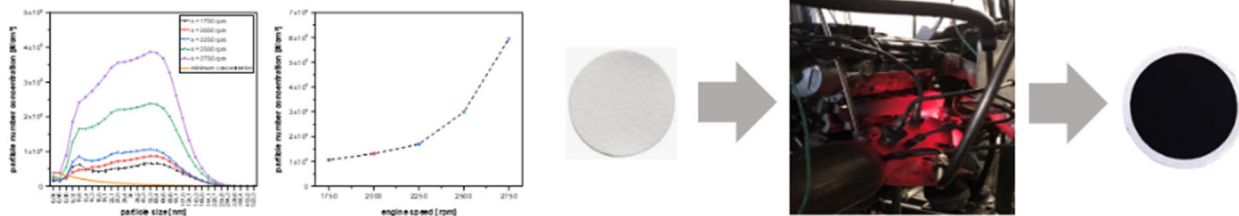
1. Variation of engine operating parameters and conditions



2. Optical analysis of internal soot formation and oxidation



3. Probing particle number and size distribution, soot sampling



4. Characterization of soot properties

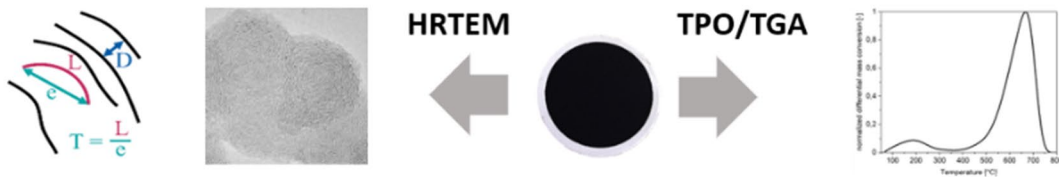


Fig. 2 Variation of global engine operating parameters and methodology of soot characterization

been determined by TPO. Both analytical techniques are briefly described in Sects. 2.5 und 2.6.

Additionally, particle number and particle size distributions within the exhaust gas were measured by an engine exhaust particle sizer (EEPS, TSI 3090). The EEPS device characterizes particle agglomerates according to their ionic mobility diameter d_m in the range from 5.6 to 560 nm with a time resolution of 10 Hz. Evaluation of the EEPS signals is performed utilizing an inversion matrix customized to soot particles from combustion engine. Besides, an AVL 419 smoke meter (SM) detects the filter smoke number (FSN). The relative error of EEPS and SM is <10 % for repeated measurements of identical engine operating points. However, the bias of the EEPS inversion matrix to translate the measured into the “true” aggregate size distribution is estimated to be larger. To complement the exhaust gas analysis, gaseous components in the exhaust gas were determined online (No. 3 in Figure 2).

The different techniques applied for characterizing GDI engine-generated particulate emissions should enable the identification of relationships between global engine operating parameters and reactivity of soot against oxidation.

2.4 Optical Analysis of In-Cylinder (In Situ) Soot Formation and Oxidation

To obtain insight into in-cylinder particle formation and oxidation, the two-color method was applied. The two-color method constitutes an established pyrometric method for determining the temporally resolved soot concentration and temperature in sooting flames [33–35]. Soot particles within a flame emit radiation over the entire electromagnetic spectrum. The spectral radiance of a soot cloud is given as

$$L_{\lambda}(\lambda, T) = \varepsilon(\lambda) L_{\lambda,s}(\lambda, T) = L_{\lambda,s}(\lambda, T_s), \quad (1)$$

where T is the temperature, λ the wavelength, $\varepsilon(\lambda)$ the dimensionless emission coefficient, and T_s the temperature of an ideal black body emitting the equivalent radiance as the nonideal radiator with $\varepsilon(\lambda) \neq 1$. The relationship between radiance of a black body $L_{\lambda,s}(\lambda, T)$ and wavelength λ at a given temperature T is given by Planck’s radiation law:

$$L_{\lambda,s}(\lambda, T) = \frac{C_1}{\lambda^5} \frac{1}{\exp\left(\frac{C_2}{\lambda T}\right) - 1} \frac{1}{\Omega_0}. \quad (2)$$

Here, C_1 and C_2 are Planck’s radiation constants and Ω_0 is the unit solid angle. Applying the law of Beer-Lambert-Bouguer, the dimensionless emission coefficient of the non-blackbody radiator, $\varepsilon(\lambda) \neq 1$, is given by

$$\varepsilon(\lambda) = 1 - \exp(-A_a c x), \quad (3)$$

where A_a is the mass specific extinction cross-section at a given wavelength, c the soot mass concentration, and x the corresponding extinction path length. By measuring the radiance at two different wavelengths ($\lambda_1 = 600$ nm and $\lambda_2 = 905$ nm), a system with two equations and two unknowns (T and c) is obtained [34, 35].

$$T = \frac{1}{\frac{1}{T_{s1}} + \frac{\lambda_1}{C_2} \ln \left\{ 1 - \left[1 - \exp\left(\frac{C_2}{\lambda_2} \left[\frac{1}{T} - \frac{1}{T_{s2}}\right]\right)\right]^{\frac{A_{a1}}{A_{a2}}} \right\}} \quad (4)$$

In Eq. (4) T_{s1} and T_{s2} are the blackbody temperatures at the wavelengths λ_1 and λ_2 , which are measured by calibration. A_{a1} and A_{a2} are the mass-specific extinction cross sections at the wavelengths λ_1 and λ_2 , which can be approximated by the absorption cross sections. Further, for deriving Eq. (4), Wien’s approximation for Planck’s radiation law is used. Once the soot particle temperature (see Eq. (4)) is known, the soot concentration can be calculated according to Eq. (5) using any of the two wavelengths:

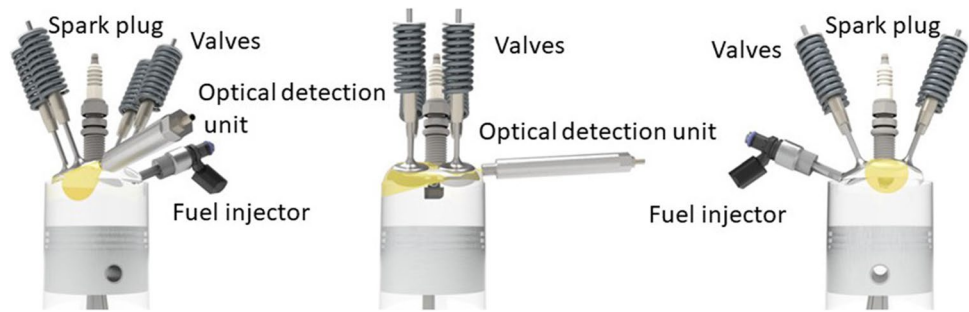
$$c = \frac{-1}{A_a(\lambda) x} \ln \left\{ 1 - \exp \left[\frac{C_2}{\lambda} \left(\frac{1}{T} - \frac{1}{T_s} \right) \right] \right\}. \quad (5)$$

This system of equations is solved iteratively. The experimental setup used for the two-color method is presented in detail elsewhere [36]. The thermal radiation of soot is detected by a fiber-coupled photodiode detection unit. By using two narrow bandpass filters with $\Delta\lambda_{FWHM} = 10$ nm bandwidth, radiation at two different wavelengths (600 nm and 905 nm) can be recorded. A tungsten lamp was used to calibrate the system and to determine T_s . Optical access to the combustion chamber was achieved by a quartz glass probe as indicated in Fig. 3. The optical probe has a conical detection volume. Therefore, only soot radiation in the combustion chamber from this probe volume can be detected. Strong cycle to cycle mixture inhomogeneities in the combustion chamber can therefore lead to a bias in the results for the measured soot concentrations. The incident soot radiation is spatially integrated and averaged over 200 engine operating cycles and three independent measurement series.

2.5 Determination of Reactivity of Soot Against Oxidation

The oxidation rates of the engine-generated soot samples were investigated ex situ through temperature programmed oxidation (TPO) in the temperature range from 300 to 800 °C. The non-isothermal, dynamic experiments have been conducted with a TG 209 F1 Libra (Netzsch Gerätebau GmbH) using a heating rate of 5 K/min and a gas mixture consisting of 95 vol.-% N_2 and 5 vol.-%

Fig. 3 Optical accessible cylinder and schematic visualization of the conical detection volume of the two-color pyrometry



O₂. Further details of the method are given elsewhere [19, 37].

The oxidation rates of soot derived from the TPO conversion profiles allow the definition of a reactivity index. On the one hand, the temperature at the maximum conversion rate, T_{max} , is frequently used to indicate reactivity against oxidation [13, 19, 38]. Low values of T_{max} are linked to high reactivity and vice versa. High soot reactivity, i.e., low T_{max} , is of benefit for an efficient GPF filter regeneration. On the other hand, reactivity can be defined with the help of a valid global overall kinetic expression for the oxidation of soot particles with a well-defined carbon nanostructure:

$$r_{ox} = \frac{d\alpha}{dT} = -\frac{k_{o,ox}^*}{\beta} \exp\left[-\frac{E_A}{Rt}\right] \alpha^{n_{ox}} = k_{0,ox} \exp\left[-\frac{E_A}{RT}\right] \alpha^{n_{ox}}. \quad (6)$$

In Eq. (6), α denotes the time-dependent soot mass normalized to the initial soot mass $m(t)/m_0$. The pre-exponential factor $k_{0,ox}$ contains the oxygen concentration, which – due to the excess – is assumed to be constant during the TPO experiment, and for $n \neq 1$ the initial mass m_0 . Further, β is the heating rate of the dynamic, non-isothermal TPO experiment, while R and n_{ox} are the universal gas constant and the overall order of the reaction. Finally, E_A describes the apparent overall activation energy of the global oxidation reaction.

As discussed in [30] and evidenced by HRTEM images, soot emitted by GDI engines consists of fractal aggregates heterogeneously composed of particles with fractions of different carbon nanostructure. The TPO conversion profiles of these soot aggregates exhibit that fractions of different nanostructure within the primary particles are oxidized independently. Oxidation of fractions with short graphene structures is associated with low T_{max} (high reactivity), and the oxidation of extended, long structures is associated with high T_{max} (low reactivity). As proposed in [37], this behavior can be described using a kinetic approach based on multiple reactants according to Eq. (7):

$$r_{ox} = \sum x_i r_{ox,i}. \quad (7)$$

Here, a three-reactant ($i = 1 \dots 3$) approach is evident from the TPO profiles; see Figure 4. The three reactants

exhibit each an individual T_{max} , indicated by the humps in the TPO profiles. The overall oxidation rate r_{ox} can be calculated applying Eq. (7), where $r_{ox,i}$ of each of the reactants is analogously given by Eq. (6). In Eq. (7), x_i describes the mass fractions of the three differently reactive soot fractions (reactants). Their associated kinetic parameters $k_{0,ox}$, n_{ox} and E_A are obviously different; see Table 4.

For substantiation of this approach, Figure 4, left part, contains the experimentally determined overall oxidation rates $-d\alpha/dT$ according to Eq. (7) of three different soot particle systems emitted by the investigated GDI engine. The operating conditions of the GDI engine for generating these particle systems are listed in Table 3.

In all TPO profiles, a low-temperature peak between 100 and 280 °C is evident, which can be attributed to the desorption and/or evaporation of volatile organic compounds (VOC) and which needs not to be considered in the discussion. This conclusion is confirmed by evolved gas analysis in the TPO experiments, where no oxidation products (CO, CO₂) can be detected within this temperature range. The soot particles represented by the green curve in Fig. 4 contain a major fraction of high reactivity ($T_{max} = 509$ °C). In contrast, the major fraction of soot particles formed at identical speed and load, but using lower injection pressure, lower relative air/fuel ratio, and double injection (red curve) exhibits low reactivity ($T_{max} = 637$ °C). The blue curve corresponds to soot particles composed of three fractions with different reactivity.

Fitting the green curve by nonlinear regression according to Eqs. (6) and (7) using a Levenberg–Marquardt least-square fitting procedure and the constraint $\sum x_i = 1$, the kinetic parameters given in Table 4 are obtained. The curves computed using the fitted parameters are indicated in Fig. 4, right part, by dashed lines. Altogether, the TPO profiles of these three soot samples point out that the aggregates generated under the listed operation parameters are composed of particles with fractions of dissimilar carbon nanostructure being oxidized independently with molecular oxygen. Obviously, for the soot samples illustrated in Fig. 4 a three-reactant approach (see Eqs. (6) and (7)) seems to be applicable.

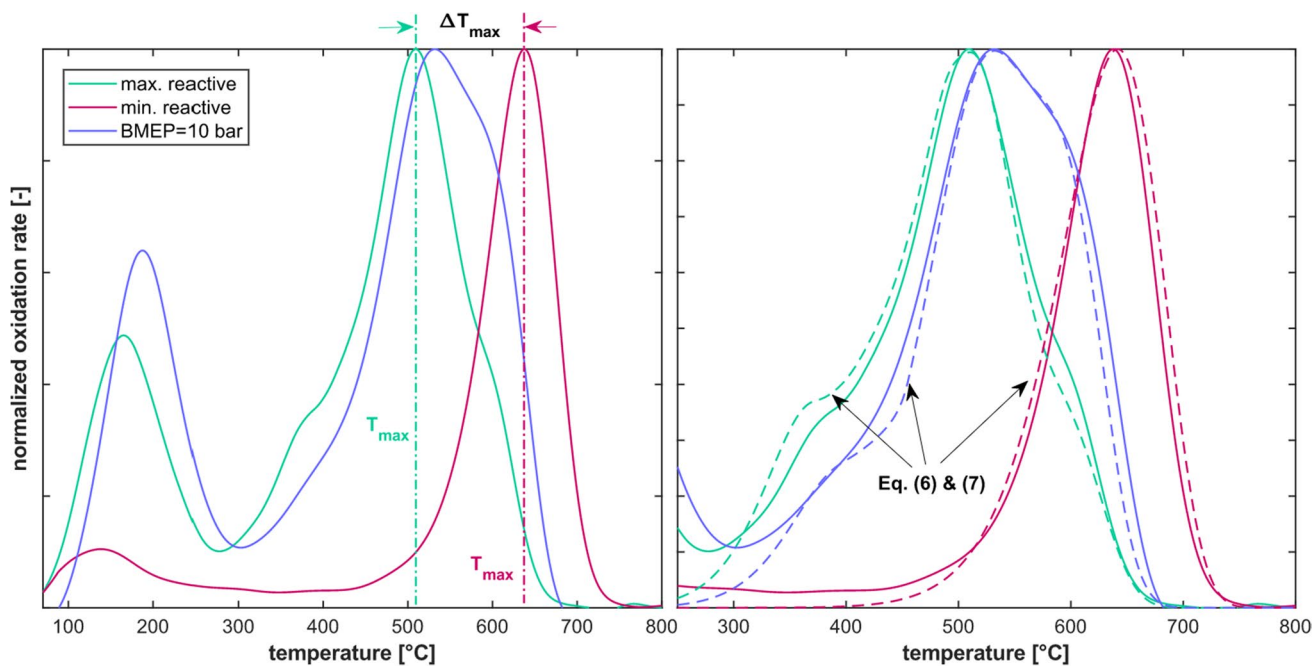


Fig. 4 Left: Experimental oxidation rates $-\dot{\alpha}/dT$ of three different selected GDI soot particle systems including markers for the determined T_{max} of the most prominent fraction. GDI engine operating

conditions are given in Table 3. Right: Enlarged profiles from the left part and calculated profiles using kinetic parameters listed in Table 4 from fitting according to Eqs. (6) and (7), dashed lines

Table 3 GDI engine operating parameters for the soot samples in Fig. 4

	n [rpm]	$BMEP$ [bar]	λ [-]	SOI [° CA BTDC]	p_{Rail} [bar]
Green curve	2000	8	1.1	310	125
Blue curve	2000	10	1	310	100
Red curve	2000	8	0.9	SOI 1: 280 EOI 2: 70	50

Table 4 Kinetic parameters from fitting the TPO profiles given in Fig. 4 (the colors of the edgings correspond to the colors of the TPO profiles in Fig. 4)

Fraction No.	X_i [-]	$k_{ox\ i}$ [$kg^{n_{ox,i}-1}K^{-1}$]	$n_{ox\ i}$ [-]	$E_{A\ i}$ [kJ/mol]
1	0.15	$2 \cdot 10^6$	1.1	94
2	0.60	$3 \cdot 10^6$	1.1	121
3	0.25	$4 \cdot 10^6$	1.0	136
1	0.08	$2 \cdot 10^6$	1.1	94
2	0.52	$3 \cdot 10^6$	1.1	121.5
3	0.40	$4 \cdot 10^6$	1.0	136
1	0.0	--	--	--
2	0.0	--	--	--
3	1.0	$4 \cdot 10^6$	1.0	145

Evidence for this approach is gained from HRTEM-images for soot particle aggregates from samples of the second operation point from Table 3. Figure 5, middle, depicts a soot aggregate containing about 200 different primary particles. From this aggregate, two cuttings are enlarged on the left side (green edging) and on the right side (yellow edging), respectively. Further enlargements are displayed in the cutting from left (blue edging) and

from right (red edging), respectively. The images with the highest resolution clearly exhibit differences of the nanostructure of the soot primary particles. While the left figure shows cuttings of primary particles with a nanostructure of low order and graphene-like structures with short extension, the right figure displays cuttings of primary particles with highly ordered nanostructure and graphene-like structures with large extension. The different nanostructure of primary soot particles contained in the aggregate presumably causes different reactivity against oxidation: Highly reactive soot particles exhibit amorphous nanostructures with short and disordered graphene layers whereas less reactive soot particles contain larger, well-ordered ones (30). Further discussion is given in Sect. 3.

For characterization of the reactivity of the soot samples listed in Table 4, three T_{max} and the corresponding mass fractions x_i of the three reactants would be necessary. The T_{max} values of the fractions with highest and lowest reactivity, respectively, of the soot samples are highlighted in Fig. 4, left, indicating a window of $\Delta T_{max} = 158$ K. However, it may be noted that oxidative conversion of the most reactive fraction

of the soot particles (fraction amounting to x_i) already commences at approx. 300 °C under the selected experimental conditions. A single T_{max} provides a global estimate of the reactivity of the particles emitted at a specific engine operating point. However, this single T_{max} is not unambiguous, if the soot contains differently reactive fractions (see blue and green TPO profiles Fig. 4). In this case, the oxidation rates according to Eqs. (6) and (7) allow a more specific definition of the reactivity via a reactivity index RI_{GDI} , which includes information about the nanostructural/molecular constitution of the soot particles. According to IUPAC [39], for the calculation of the reactivity index, the oxidation rate under certain reaction conditions is considered. As proposed in [40], RI_{GDI} is defined using the overall oxidation rates according to Eq. (7) of the different soot samples at 527 °C and 5 vol.-% O_2 at 50 % mass conversion ($\alpha=0.5$) of the sample. To cover a range of $0 \leq RI_{GDI} \leq 1$, this reaction rate is normalized with the reaction rates of the fractions of soot particles with maximum and minimum reaction rate from Fig. 4. The RI_{GDI} calculated in this way due to the normalization lies between 0 (min. reactive) and 1 (max. reactive):

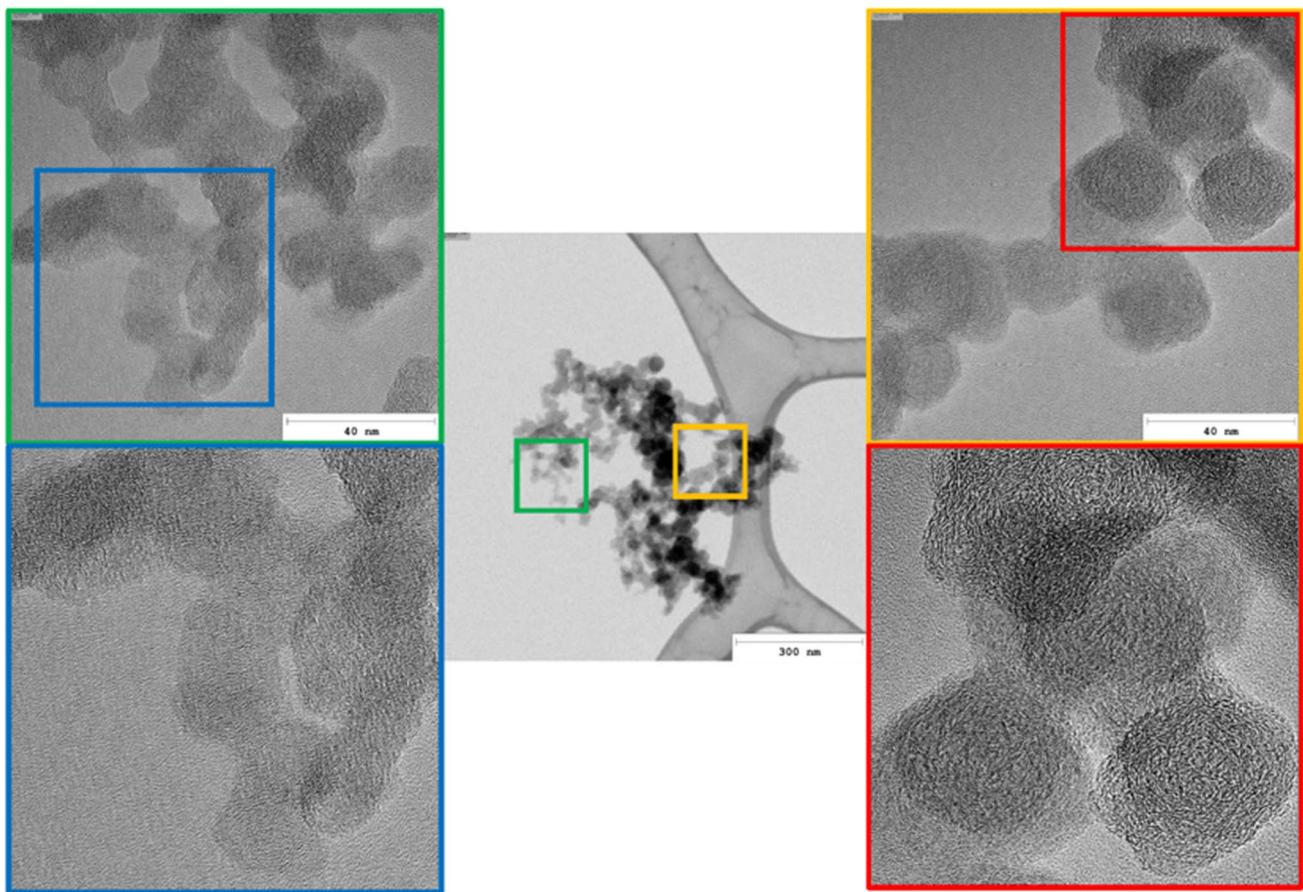


Fig. 5 HRTEM images of a soot sample aggregate sampled at $BMEP=10$ bar with enlargement at two different positions indicating different nanostructural details of the respective primary particles

$$RI_{GDI} = \frac{\left[\ln\{r_{ox,min}\} - \ln\{r_{ox,GDI}\} \right]}{\left[\ln\{r_{ox,min}\} - \ln\{r_{ox,max}\} \right]} \quad T = 800 \text{ K}, \alpha = 0.5, 5 \text{ vol.} - \% \text{ O}_2 \quad (8)$$

The green curve plotted in Figure 4 gives a reactivity index $RI_{GDI} = 1$, while the blue curve yields $RI_{GDI} = 0.71$. In contrary, T_{max} of the most prominent fractions (x_2) in the two particle types differs by only 22 °C. This results from the inclusion of the oxidation rates of all fractions into the calculation of RI_{GDI} , particularly the nonreactive carbon fraction with $x_3 = 0.25$ and $x_3 = 0.40$, respectively, and an activation energy of $E_{A,3} = 136 \text{ kJ/mol}$, $k_{0,ox,3} = 4 \cdot 10^6 \text{ K}^{-1}$, $n_{ox,3} = 1.0$. Consequently, the oxidation behavior is not reflected by only one single T_{max} . Instead, the single parameter RI_{GDI} according to Eq. (8) provides a measure of the reactivity including implicitly the T_{max} of the different reactants. It also considers the initiation of the oxidation at approx. $T > 300^\circ\text{C}$ and the different reactivity behavior of the different fractions composing GDI-generated soot aggregates.

2.6 Characterization of Micro- and Nanostructural Soot Properties

In this study, HRTEM is used to evaluate morphological and nanostructural particle characteristics. The electron microscope (Philips CM200 transmission electron microscope, ThermoFisher Scientific Inc.) is operated at 200 kV and a maximum magnification of 380.000 resulting in highest spatial resolution of 0.0283 nm/px [19, 41]. The TEM grid preparation was performed similar to Koch et al. (30). The top layer of quartz fiber filters on which soot particles are deposited was carefully removed, mixed with high purity water, stirred and after multiple filtration steps deposited on carbon-coated cooper TEM grids. A total of 30–50 TEM images were acquired per engine operating parameter.

The HRTEM image analysis algorithms to analyze the primary particle size distributions as well as the carbon nanostructural characteristics are described in detail in [19, 41]. The HRTEM image analysis algorithm to quantify nanostructural characteristics is based on Yehliu et al. [42]. The basic steps of the algorithm are filtering in the Fourier space, image comparison, top-hat transformation, binarization, skeletonizing elements using Zhang-Suen algorithm [43], post-processing of the skeletons, and analysis of nanostructural characteristics, i.e., the calculation of the fringe length distribution [19]. The HRTEM image analysis algorithm evaluates the nanostructure of 50 to 300 primary particles from different HRTEM images of the same soot sample, enabling the quantification of > 10,000 fringes [40].

Figure 6, top, shows exemplarily the primary particle size distribution for the engine operating point at $\lambda = 0.7$, $n = 2000 \text{ rpm}$, and $BMEP = 8 \text{ bar}$. The analyzed primary particles cover a diameter range of $3 \text{ nm} \leq d_{pp} \leq 50 \text{ nm}$ and their size distribution can be approximated best by a logarithmic normal distribution according to Eq. (9). The size distribution plotted in Figure 6 yields a count median diameter of $CMD=21 \text{ nm}$ and a geometric standard deviation $\sigma_g = 1.44$:

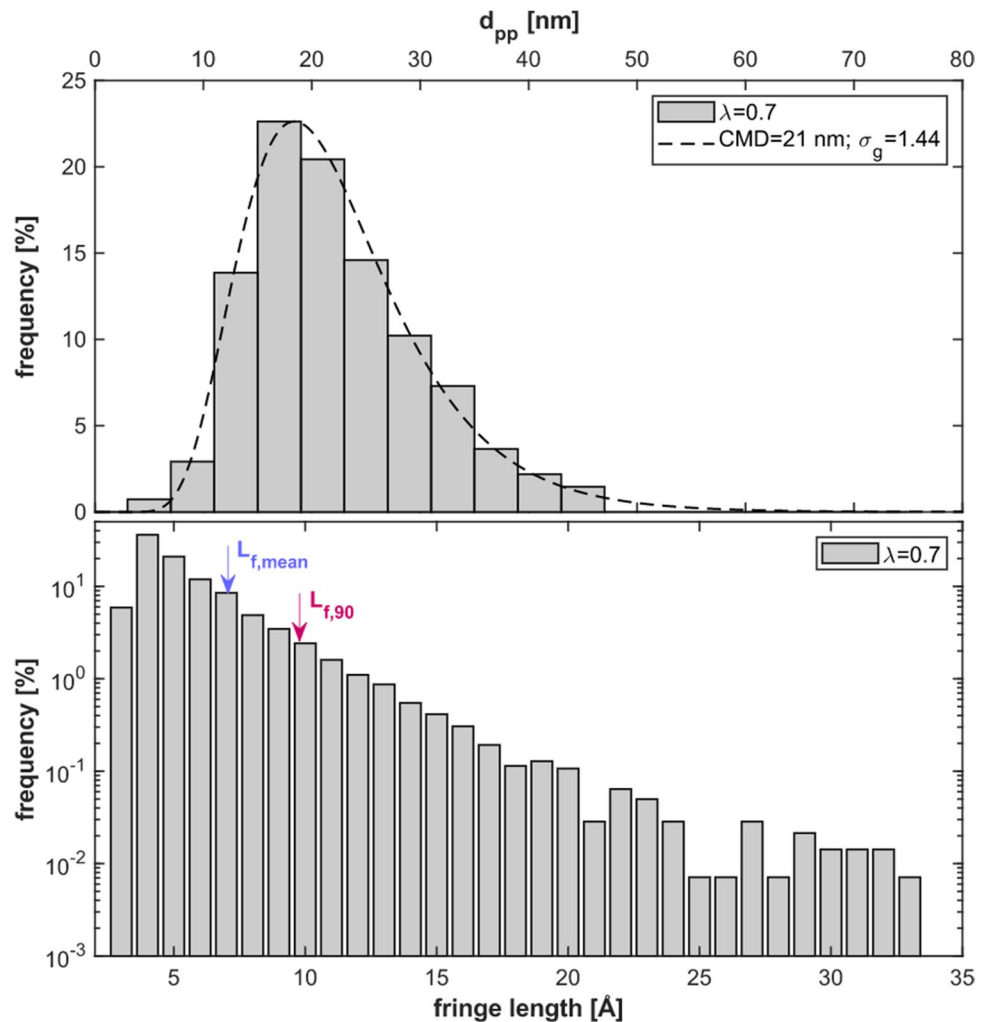
$$P(d_{pp}) = \frac{1}{\sqrt{2\pi} d_{pp} \ln \sigma_g} \exp \left\{ -\frac{(\ln d_{pp} - \ln CMD)^2}{2 (\ln \sigma_g)^2} \right\} \quad (9)$$

The carbon nanostructure encompasses the collocation of layered graphene-like structures distinguished by their length, curvature, and separation distance as well as defects within the crystallite structure. In principle, the HRTEM image analysis algorithm introduced in [41] and [19] allows the quantification of the size L_f , curvature T_f , and separation distance $D_{s,f}$ of the graphene-like structures (fringes) embedded within primary particles. As worked out in [19, 40], the fringe length L_f affects soot reactivity to the most part. Therefore, only L_f is presented in this study. Figure 6, bottom, shows the fringe length distribution evaluated via HRTEM image analysis algorithm for the same engine operation point. Fringes ranging from 2.5 to 35 Å are detected, with an arithmetic mean $L_{f,mean} = 5.5 \pm 0.2 \text{ Å}$ and a decile corresponding to $L_{f,90} = 8.3 \pm 0.5 \text{ Å}$. It should be noted that the evaluation of the HRTEM images visualizes the different fractions of soot within the soot particles and, therefore, the evaluated nanostructural parameters contain contributions from all structures captured by the image analysis algorithm.

3 Results and Discussion

To assess the effect of global engine operating parameters on soot oxidation by oxygen at moderate temperatures, the GDI engine used in this work was operated under different operating conditions, which, on the one hand, strongly differ in engine speed and torque at stoichiometric overall mixture composition ($\lambda = 1$) and homogeneous combustion mode. On the other hand, the relative air/fuel ratio has been varied ($\lambda \neq 1$) in a steady-state operating point. First, the general impact of engine speed is discussed. This is followed by results and

Fig. 6 Primary particle size distribution (top) and fringe length distribution (bottom) for $\lambda=0.7$, $n=2000$ rpm, and $BMEP=8$ bar analyzed via HRTEM and image analysis algorithms



discussion of the impact of engine torque ($BMEP$) and relative air/fuel ratio on the characteristics of the generated soot particles and the reactivity against oxidation. Table 2 contains the variations of the engine parameters conducted in this study.

3.1 Influence of Engine Speed on Particle Concentration and Reactivity

Without adjustment of camshaft timings and, consequently, flow conditions, the mixture homogenization of fuel and air generally strongly depends on the speed of rotation and the turbulence generated thereby. Therefore, the engine speed was varied in the range from 1750 to 2750 rpm at constant indicated engine load ($IMEP=9$ bar) and constant further engine parameters. The constant fuel mass was injected with a single injection ($SOI=310^\circ$ CA BTDC) and constant injection pressure ($p_{Rail}=100$ bar) in stoichiometric, homogeneous operating mode. The effect of engine speed variation on

particle size distributions, number concentrations, and soot reactivity are given below.

3.1.1 Particle Number Concentrations and Size Distributions

Figure 7, left part, presents aggregate size distributions as measured with the help of the EEPS and the total particle number (PN) concentration in dependence of engine speed. The size distributions as measured with the EEPS are by way of a hint bimodal, and a shift of the size distributions towards accumulation mode and larger mean aggregate diameter with higher speed of rotation can be observed. As can be seen from Fig. 7, right part, the total particle number concentration increases reasonably with ascending engine speed.

The reason for the observed dependencies is, on the one hand, the shorter time for mixture formation leading to inhomogeneities of the air-fuel mixtures, unless the remaining engine operating parameters are adjusted. On the other hand,

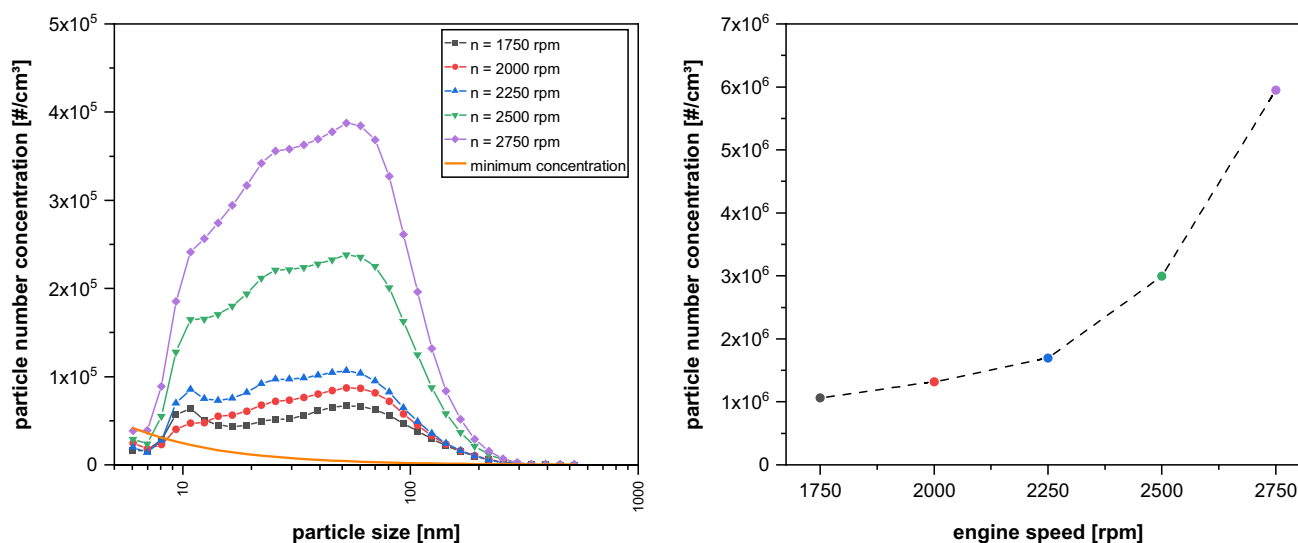


Fig. 7 Mobility particle size distributions and total particle number concentrations at various engine speed n (IMEP=9 bar, $\lambda=1$); orange curve represents the detection limit of the EEPS

higher engine speed causes shorter residence times of the formed soot particles inside the cylinder and therefore a shorter high-temperature post-flame oxidation period.

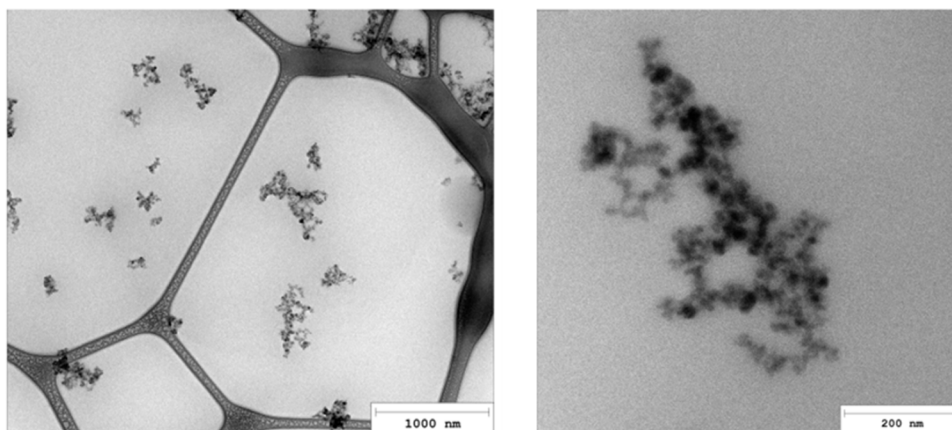
Figure 8 displays TEM images of soot particle aggregates collected directly on TEM grids in the exhaust gas at the operating point with $n = 2000$ rpm. On the one hand, the TEM images clearly indicate soot particle aggregates with widely varying sizes reflecting the broad size distributions as depicted in Fig. 7. The size of the primary particles in the aggregates is in the order of magnitude measured by the evaluation of HRTEM images (CMD about 20 nm, see Fig. 6). On the other hand, aggregate sizes measured with the help of the EEPS (see Fig. 7) appear to be significantly smaller than the ones noticeable on the TEM images. These differences can be attributed to the conversion of EEPS signals into mobility diameters of the aggregates. The conversion method

underestimates the mobility diameters considerably (44). Applying estimates for the conversion of the mobility diameters d_m into diameters of gyration d_R given in [45], yields $d_R \approx 1.3 d_m$. From that, the EEPS aggregate sizes appear reasonably smaller than the aggregates characterized by the diameter of gyration, which is the parameter reflected from the TEM-images.

3.1.2 Reactivity Against Oxidation

Figure 9, left part, shows the normalized differential mass conversion rates for the TPO of soot samples generated under different engine speeds. As discussed in Section 2.5, the peak at low temperatures is caused by the evaporation of highly volatile components and is not considered here. The results from the TPO analysis exhibit only minor differences in the over-all oxidation

Fig. 8 Soot aggregates collected at $n=2000$ rpm and $BMEP=8$ bar in-situ on TEM-grids in the exhaust gas



rates and only minor differences concerning the fractions of dissimilar carbon nanostructure within the soot particles. This can be recognized by the approximately equal oxidation rates and temperatures at maximum oxidation rate T_{max} for the different fractions. T_{max} for the most prominent fraction varies only by about 5 °C and the reactivity index RI_{GDI} given by Eq. (8) changes by about 12 %; see Figure 7, right part.

In spite of the increasing total particle number concentration and particle sizes, values of T_{max} and RI_{GDI} for the engine speed range considered are at a similar level. An increase in engine speed tends to the formation of little less reactive soot, as indicated by a slowly decreasing RI_{GDI} and a rising value of T_{max} and a slight shift of the conversion to higher temperatures ($n > 2500$ rpm). This is consistent with results reported in [30], indicating lower reactivity of soot particles formed in mixtures with lower degree of homogenization. Further, at higher engine speed, $n > 2250$ rpm, the formation of an additional fraction of only low reactivity is obvious as indicated by the evolution of a shoulder in the TPO profiles at higher temperatures. This is reflected by the kinetic parameters and the proportion of the different fractions calculated by least square fitting of the TPO profiles from Figure 9 according to Eqs. (6) and (7) applying a three-reactant approach; see Table 5. The amount of the most nonreactive soot fraction (x_3) increases with increasing engine speed, as well as the apparent activation energy for the oxidation of this fraction ($E_{A,3}$).

In contrast to variations of engine load and relative air/fuel ratio discussed below, variations of engine speed have only a minor influence on the reactivity of soot against oxidation. Since no significant differences in soot oxidation

behavior could be observed, HRTEM and in-cylinder optical studies at these operation points were not conducted.

3.2 Influence of Engine Load and Thermodynamic Boundary Conditions on In-Cylinder Soot Formation, Soot Emission, Reactivity, and Nanostructure of Soot

In this section, the impact of $BMEP$ and engine load (torque) on soot particle characteristics is considered, and a correlation to reactivity of soot against oxidation is established. One of the main sources of particle formation in non-stratified mode are pool fires. In order to minimize fuel impingement on the piston and subsequent pool fires, the single injection is initiated at an optimal injection timing of $SOI = 310$ °CA BTDC. In addition, the experimental findings are supported by in situ optical investigations of in-cylinder soot formation and oxidation and ex situ analysis of carbon nanostructure and primary particles size distributions of soot aggregates. Table 2 gives the parameter settings of the engine load variation.

3.2.1 Thermodynamic Analysis of Engine Load Variation

The thermodynamic analysis of engine load change from low to high $BMEP$ at constant engine speed $n = 2000$ rpm and air/fuel ratio $\lambda = 1$ is given in Figure 10. As expected, an increase in engine load (torque) due to higher amount of injected fuel and air consequently leads to higher combustion pressures (in-cylinder pressures) and faster increases of pressure and temperatures and higher and faster heat releases. In case of the highest engine torque, a combustion temperature of 2400 °C and a pressure of 67 bar are attained.

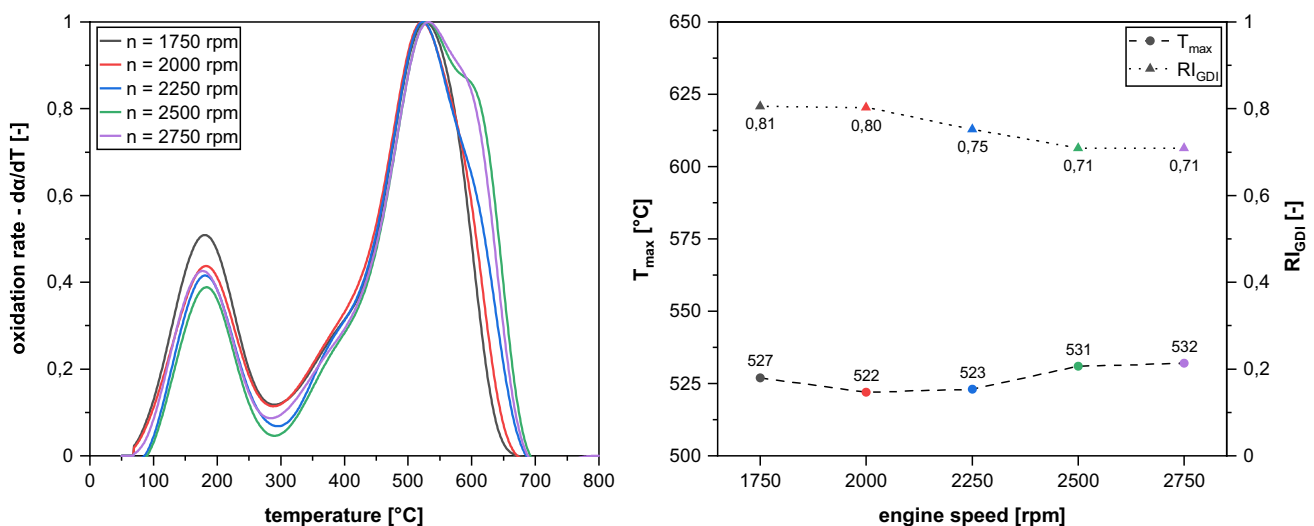


Fig. 9 Experimental oxidation rates $-d\alpha/dT$ of soot samples (left part) and T_{max} for the most prominent fraction of soot as well as reactivity index RI_{GDI} (right part) at various engine speeds n (IMEP=9 bar, $\lambda = 1$)

Table 5 Kinetic parameters for the oxidation of soot samples from engine speed variations (IMEP = 9 bar, $\lambda = 1$)

n [rpm]	x_I [%]	$k_{0,ox,I}$ [$\text{kg}^{\text{thex,3-1}} \text{K}^{-1}$]	$E_{A,I}$ [kJ/mol]	$n_{ox,I}$ [-]	x_2 [%]	$k_{0,ox,2}$ [$\text{kg}^{\text{thex,2-1}} \text{K}^{-1}$]	$E_{A,2}$ [kJ/mol]	$n_{ox,2}$ [-]	x_3 [%]	$k_{0,ox,3}$ [$\text{kg}^{\text{thex,3-1}} \text{K}^{-1}$]	$E_{A,3}$ [kJ/mol]	$n_{ox,3}$ [-]	R/GDI [-]
1750	10	$2 \cdot 10^6$	99	1.1	45	$3 \cdot 10^6$	121	1.1	45	$4 \cdot 10^6$	133	1.0	0.81
2000	10	$2 \cdot 10^6$	99	1.1	45	$3 \cdot 10^6$	121	1.1	45	$4 \cdot 10^6$	135	1.0	0.80
2250	7	$2 \cdot 10^6$	99	1.1	48	$3 \cdot 10^6$	121	1.1	45	$4 \cdot 10^6$	137	1.0	0.75
2500	7	$2 \cdot 10^6$	100	1.1	42	$3 \cdot 10^6$	123	1.1	51	$4 \cdot 10^6$	139	1.0	0.71
2750	7	$2 \cdot 10^6$	100	1.1	42	$3 \cdot 10^6$	123	1.1	51	$4 \cdot 10^6$	139	1.0	0.71

In this series of experiments, the ignition timing is variable and controlled for an optimum combustion efficiency ($MFB50 = 8$ °CA ADTCf). An exception here is the highest engine load point, $BMEP = 12$ bar. Due to the occurrence of engine knocking, the ignition was delayed in this case as visible from the retarded increase of combustion pressure, temperature, and heat release.

3.2.2 Optical Investigation of In-Cylinder Soot Formation and Oxidation

Figure 11 presents the findings of in-cylinder soot formation and oxidation as a function of $BMEP$ monitored with the two color pyrometry. The in-cylinder concentration of soot increases during the working cycle, attains a maximum and decreases again due to almost complete soot oxidation in the late phase of the working cycle. Growing mixture inhomogeneities inside the cylinder as a result of increasing fuel and air quantities lead to a significant increase of the amounts of soot being formed. With increasing $BMEP$, the maximum soot concentrations increase, and its occurrence is shifted towards late combustion (20–40 °CA ATDC). The later attainment of the maximum soot concentrations can be attributed to a higher formation rate of soot. The fraction of soot surviving the oxidation in the late phase of the working cycle increases also with increasing $BMEP$. Only the measured soot concentration at $BMEP = 10$ bar (–20 °CA ATDC to approx. 70 °CA ATDC) falls out of that line. However, the curve for 10 bar later than approx. 70 °CA ATDC matches the curves at lower pressures. A random error can be ruled out since profiles were reproduced in three independent measurement series. The reason for this lies in probably strong mixture inhomogeneities with increasing amounts of air and injected fuel. However, a quantitative interpretation is limited, because possibly only a part of the generated soot radiation can be detected in the fixed probe volume inside the cylinder; see Fig. 3. A further source of bias lies in the two-color pyrometry, which detects radiation from only hot soot particle with significant thermal radiation in the red and near-infrared spectral region. Soot particle clouds being cooled down to lower temperatures in colder areas of the inhomogeneous mixture, do not contribute to the emitted radiation. Also, the pressure and temperature dependence of the chemical reaction rates for the formation and oxidation of soot contribute to these trends.

3.2.3 Exhaust Particle Number Concentration, Particle Size Distributions, and Gaseous Components

Figure 12 shows the total particle number concentration (PN) (right part) and aggregate size distributions (left

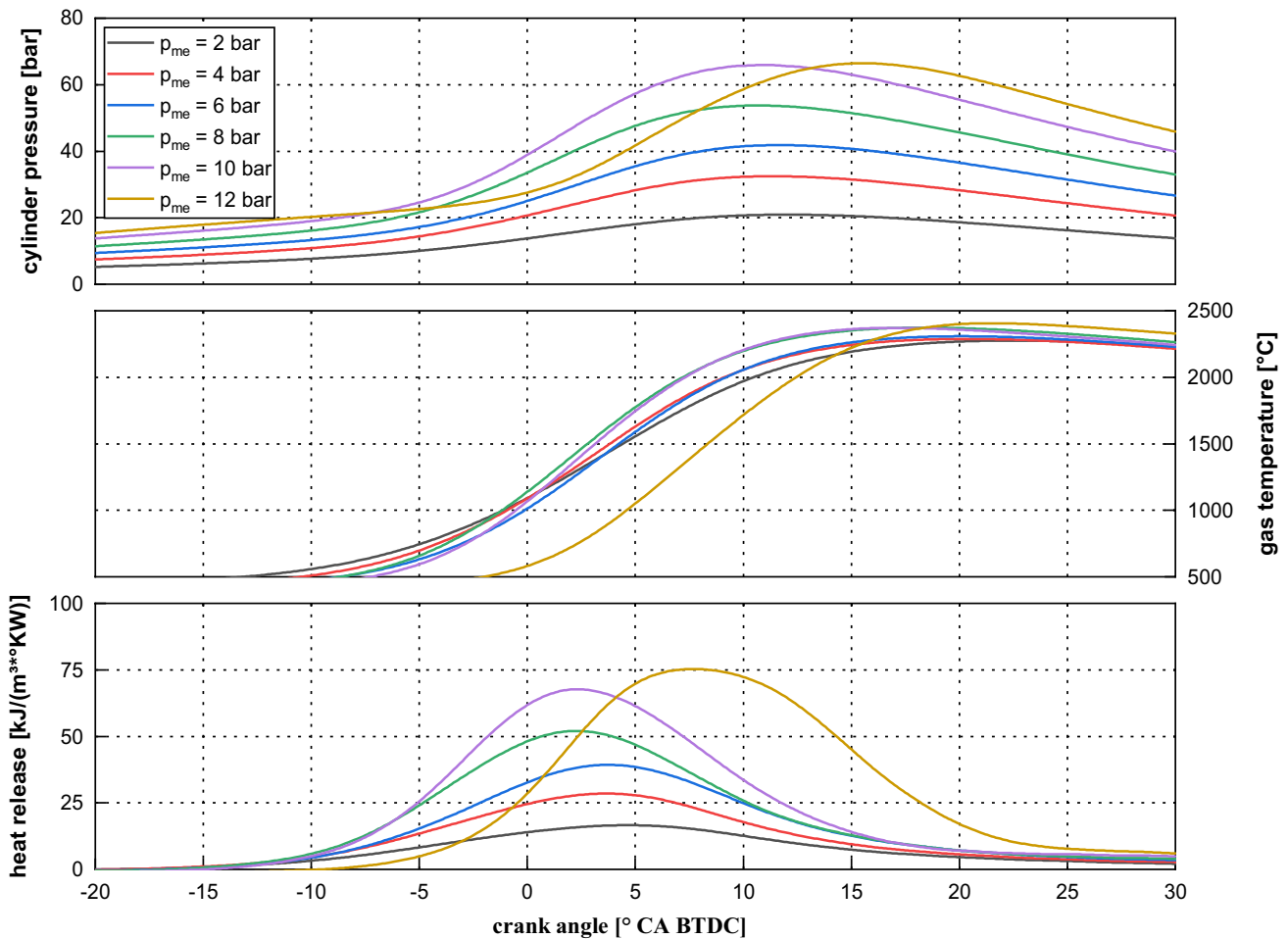


Fig. 10 Thermodynamic analysis of engine load variation (*BMEP*) ($n=2000$ rpm, $\lambda=1$)

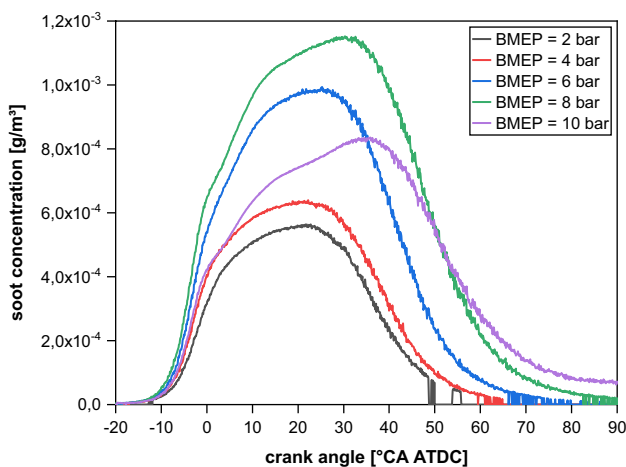


Fig. 11 In-cylinder soot mass concentration as function of crank angle for varying engine loads ($n=2000$ rpm, $\lambda=1$) determined via two-color pyrometry

part) measured in the exhaust as a function of *BMEP*. In spite of the same injection strategy, the effect of increasing fuel and air mass injected into the cylinder to achieve higher torque of the engine is evident in the particle number concentration and size distributions.

Similar to the distributions presented in Fig. 7, the aggregate size distributions as measured by EEPS are bimodal with a shift of size distributions towards accumulation mode and larger mean aggregate diameters with higher *BMEP*. TEM images of aggregates collected at different pressures on quartz fiber filters are composed in Fig. 13. The TEM images illustrate comparatively large aggregates and primary particles with sizes in the order of magnitude of 20 nm. The bimodal shape of the size distribution of the aggregates deviates from that of the primary particles; compare Fig. 6. For the discussion of the apparent differences in the aggregate sizes from EEPS and TEM images, see Sect. 3.1.1. Favored by the increasing combustion pressure and the associated increased reaction rates, the process of soot

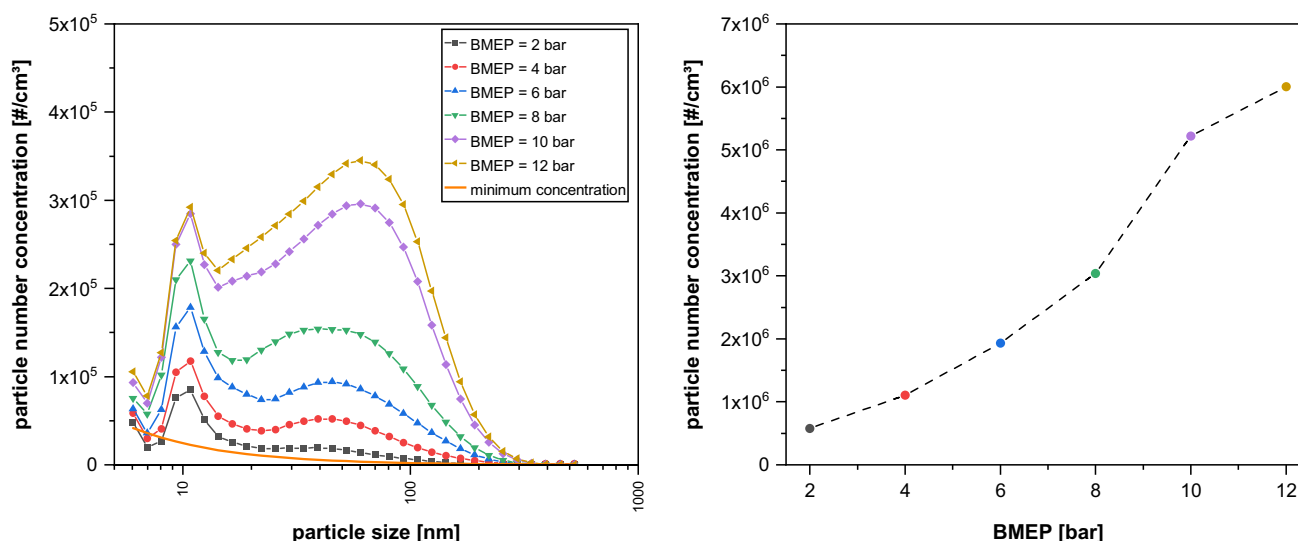


Fig. 12 Mobility size distributions and total number concentrations at various engine loads ($n=2000$ rpm, $\lambda=1$); the orange curve represents the detection limit of the EEPS

formation is sustained for longer and the proportion surviving oxidation in the late phase of the working cycle increases. For this reason, an increase of combustion pressure leads to larger soot particle aggregates and an increased soot concentration and number concentration inside the cylinder (see Fig. 11) and in the exhaust.

Figure 14 exemplifies the exhaust gas emissions for this parameter variation. Analogous to the total particle number concentration measured by EEPS, the exhaust soot mass concentration represented by the FSN increases with higher engine load. With increasing pressure, the exhaust concentration of total hydrocarbons decreases.

3.2.4 Reactivity Against Oxidation

Normalized TPO profiles of soot samples generated under different combustion pressures and temperatures are given

in Figure 15. The peaks in the TPO profiles at temperatures below approximately 250 °C are caused by the evaporation of VOCs. The amounts of VOCs relative to the total amounts of the TPO sample decrease with increasing pressure. The oxidation rates can be well described with the help of a three-reactant approach omitting the evaporation of highly volatile components at low temperatures. The reactivity index decreases with increasing *BMEP*. Similar observation has been made for diesel soot [28].

Low *BMEP* causes a high degree of homogenization of fuel and air, resulting in low particle number concentrations of small aggregates and particle size distributions with a comparatively low peak in the accumulation mode; see Fig. 12. The particles exhibit high reactivity as evidenced by the kinetic parameters and the reactivity index RI_{GDI} listed in Table 6. As the engine load increases, the proportion of the fraction of highly reactive particles (x_I) decreases.

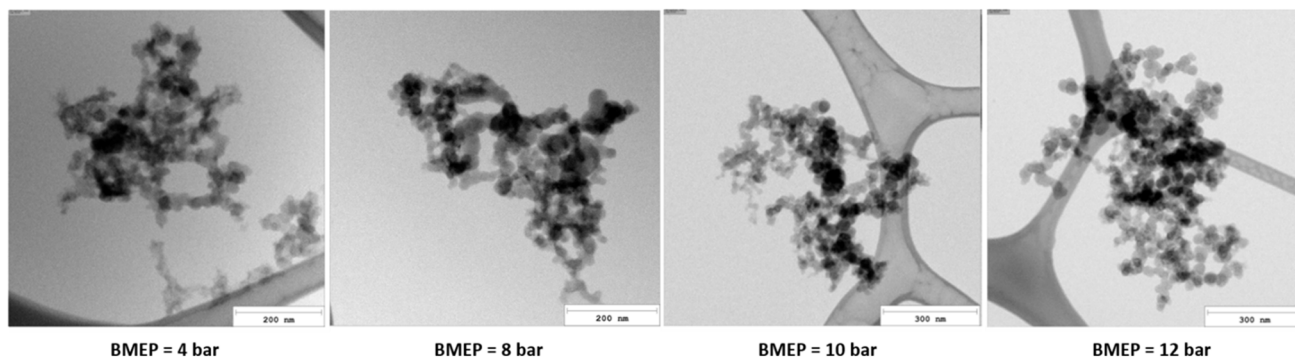


Fig. 13 Soot particle aggregates collected at variation of engine load at $n=2000$ rpm on quartz fiber filters; note the different scales at low pressure (4 bar and 8 bar) and higher pressure (10 bar and 12 bar)

Fig. 14 Filter smoke number (FSN) and hydrocarbon concentration of the engine load variation (engine speed = 2000 rpm, $\lambda = 1$)

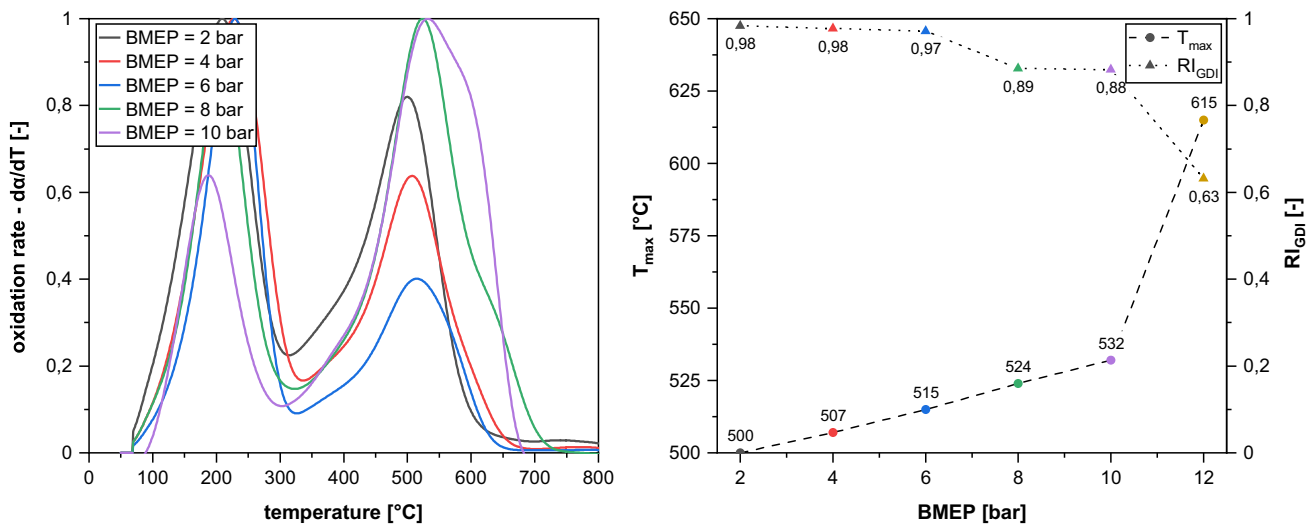
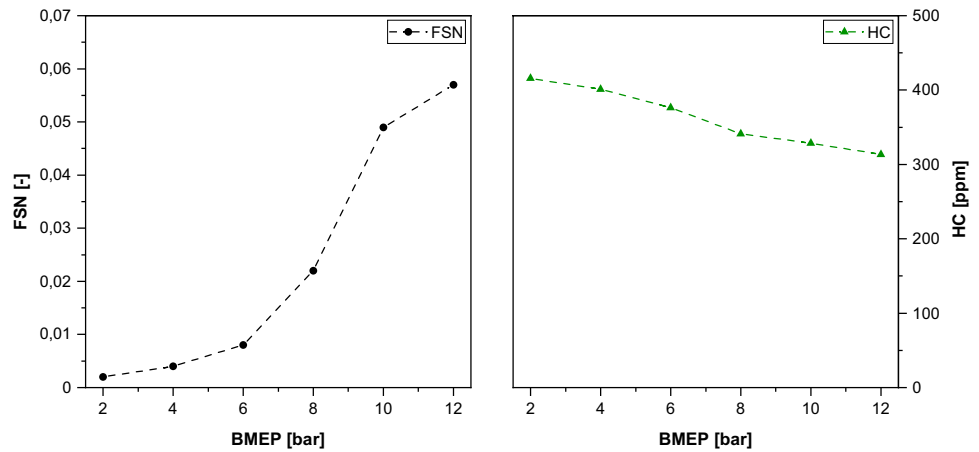


Fig. 15 Experimental oxidation rates $-d\alpha/dT$ of soot samples (left part) and T_{max} for the most prominent fraction of soot as well as reactivity index RI_{GDI} (right part) at various engine loads $BMEP$, $n=2000$ rpm, $\lambda=1$

Simultaneously, the proportion of the less reactive fraction of soot (x_3) increases significantly at $BMEP$ higher than 6 bar. The apparent activation energy $E_{A,3}$ of this soot type ($E_{A,3}$) is about 132 to 141 kJ/mol. In case of the highest $BMEP$ with delayed ignition timing and combustion, the nonreactive soot type with $T_{max}=615$ °C is generated in high amounts, see Table 6, with $x_3=83$ % at the highest $BMEP$.

The results obtained by engine load variations suggest that soot generated at low and middle $BMEP$ inside the cylinder is more or less completely oxidized in later phase of combustion resulting in low exhaust particulate emission (FSN) of soot with large proportions of the fractions with high reactivity; see Figs. 14 and 15. Further, elevated soot concentrations generated at high $BMEP$ in the cylinder and remaining in the exhaust gas as measured by the two-color method, EEPS and smoke meter, consist of increasing proportions of fractions of nonreactive soot particles with low RI_{GDI} and high T_{max} values.

Choi et al. [32] attribute the GDI soot reactivity mainly to catalytic effects. As known from diesel engine combustion, catalytically active ash particles are embedded in soot aggregates due to increased oil combustion. The embedded ash particles containing metal oxides and metal phosphates can act as oxidation promoters [25], resulting in a significant increase of the reactivity of soot regardless of the engine operating condition. In this study, however, no measurable oil consumption was detected during the experiments. In addition, to avoid cross-influences, the experiments on the influence of the global engine operating parameters and the resulting combustion process on soot reactivity were carried out with an external crankcase ventilation system. It should also be noted that the oil analyses carried performed for the tested engine showed a very low ash content of less than 1 wt.-% and wear elements in the normal range, even after 30,000 km of operation.

Table 6 Kinetic parameters for the oxidation of soot samples from engine load variations ($n = 2000$ rpm, $\lambda = 1$)

$BMEP$ [bar]	x_1 [%]	$k_{0,ox,1}$ [$\text{kg}^{0.05,1} \text{K}^{-1}$]	$E_{A,1}$ [kJ/mol]	$n_{ox,1}$ [-]	x_2 [%]	$k_{0,ox,2}$ [$\text{kg}^{0.05,2} \text{K}^{-1}$]	$E_{A,2}$ [kJ/mol]	$n_{ox,2}$ [-]	x_3 [%]	$k_{0,ox,3}$ [$\text{kg}^{0.05,3} \text{K}^{-1}$]	$E_{A,3}$ [kJ/mol]	$n_{ox,3}$ [-]	RI_{GDI} [-]
2	15	$2 \cdot 10^6$	95	1.1	65	$3 \cdot 10^6$	119	1.1	20	$4 \cdot 10^6$	132	1.0	0.98
4	15	$2 \cdot 10^6$	95	1.1	60	$3 \cdot 10^6$	120	1.1	25	$4 \cdot 10^6$	133	1.0	0.98
6	15	$2 \cdot 10^6$	95	1.1	60	$3 \cdot 10^6$	122	1.1	25	$4 \cdot 10^6$	135	1.0	0.97
8	8	$2 \cdot 10^6$	94	1.1	63	$3 \cdot 10^6$	123	1.1	29	$4 \cdot 10^6$	141	1.0	0.88
10	8	$2 \cdot 10^6$	94	1.1	40	$3 \cdot 10^6$	121.5	1.1	52	$4 \cdot 10^6$	136	1.0	0.88
12	2	$2 \cdot 10^6$	94	1.1	15	$3 \cdot 10^6$	121	1.1	83	$4 \cdot 10^6$	141	1.0	0.63

Clean combustion of a homogeneous mixture is obviously advantageous for generating reactive particles that can be oxidized rapidly during GPF regeneration. More insight into the cause of variation of soot reactivity can be gathered by micro- and nanostructural analysis of soot particles presented in Sect. 3.2.5.

3.2.5 Carbon Nanostructure and Size Distributions of Primary Particles

Figure 16 summarizes the results of the carbon nanostructure analyses and primary particle size distribution analyses for the experiments with $BMEP$ variation. It should be noted that the evaluation of the HRTEM images captures the different fractions of soot within the soot particles. Therefore, the values of the nanostructural parameters discussed below include integral values over the different fractions. The analyzed count median diameter CMD ranges between 25.5 and 29.7 nm with a geometric standard deviation σ_g between 1.34 and 1.50; see Figure 16, bottom left part. These values correspond to the values reported in the literature, e.g. [40, 41], and [44].

Further, primary particle size distributions represented by the CMD and σ_g do not change systematically as a function of $BMEP$. The increasing soot concentration is reflected in the larger aggregate size containing a larger number of primary particles. Conversely, the mean fringe length, $L_{f,mean}$, and the decile of the fringe length distribution, $L_{f,90}$, increase gradually with increasing $BMEP$; see Fig. 16, upper left. From that, it can be concluded that the carbon nanostructure of the primary particles evolves to an increasingly graphitized state with increasing $BMEP$, while the primary particle sizes remain approximately constant. In [19], it was demonstrated that $L_{f,mean}$ correlates excellently with the reactivity against low temperature oxidation by molecular oxygen. This dependence can be verified by plotting $L_{f,mean}$ and $L_{f,90}$ versus the reactivity index RI_{GDI} , Fig. 16, top right. With increasing $BMEP$, the fringe length grows, resulting in a RI_{GDI} decrease. This can be attributed to a growing CH ratio with increasing fringe lengths implying a decrease of the relative number of C-H edge sites of the graphene-like structures or fringes accessible for oxidation. In contrast, no systematic dependency of the reactivity index RI_{GDI} on CMD or σ_g can be found; see Fig. 16, bottom right.

From the results, it can be concluded that increased combustion temperatures and pressures, as well as progressively more inhomogeneous air–fuel mixtures, not only increase the number concentration and aggregate size of the soot particles formed, but also increase the length of fringes embedded within primary particles. In contrast, primary particle size distributions remain largely unchanged. Since fringe length significantly affects soot reactivity, RI_{GDI} successively decreases (T_{max} increases) with increasing $BMEP$.

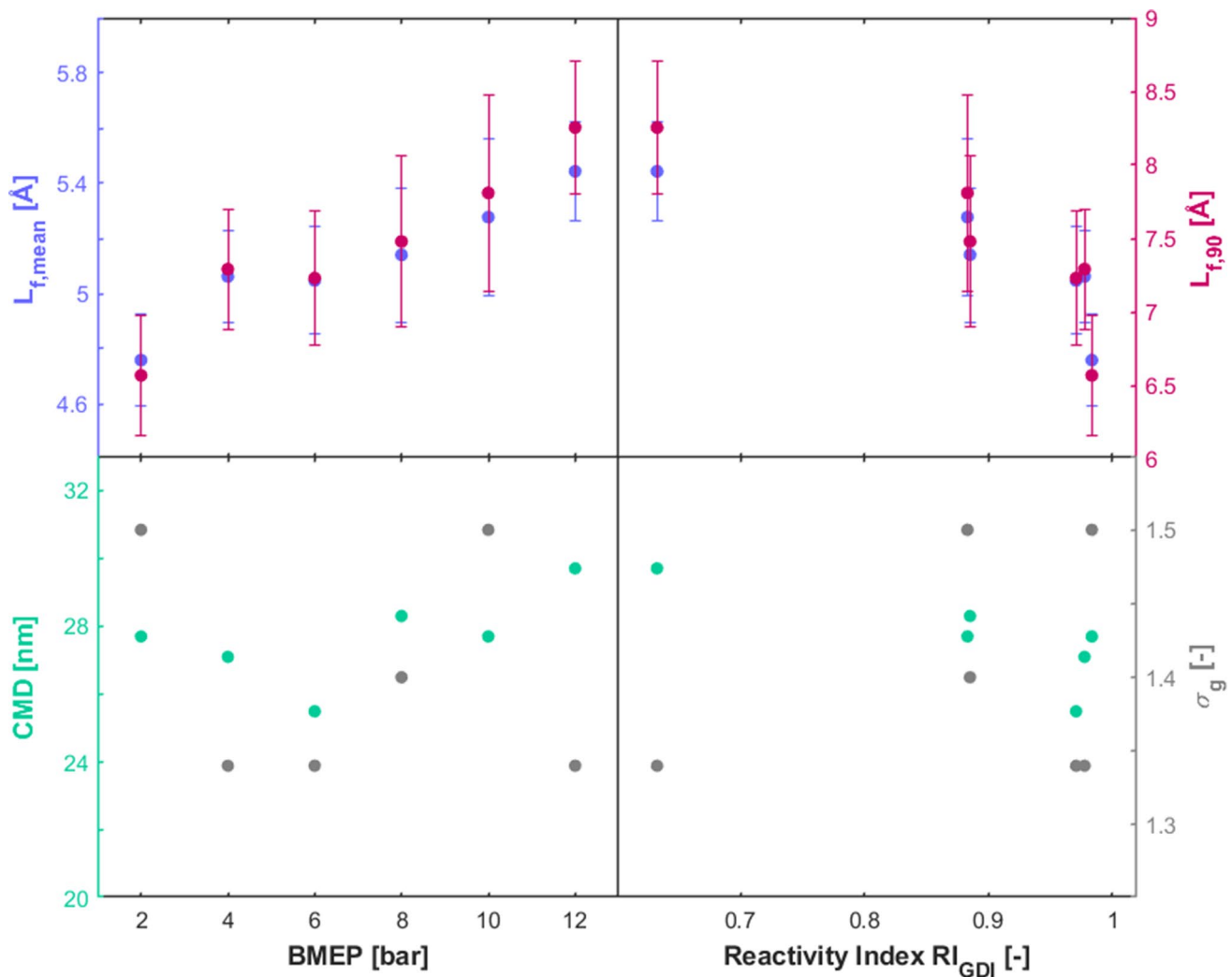


Fig. 16 Mean fringe length (blue symbols) and decile of the fringe length distributions (red symbols), upper part, as well as count median diameter (CMD, green symbols) and geometric standard devi-

ation of primary soot particle size distributions (grey symbols), lower part, plotted versus *BMEP* (left) and RI_{GDI} (right), $n=2000$ rpm, $\lambda=1$

3.3 Variation of Relative Air/Fuel Ratio: Influence on Particle Characteristics

In the following, the influence of relative air/fuel ratio λ at a steady-state operating point ($n = 2000$ rpm, $BMEP = 8$ bar) on particle properties and consequently on soot reactivity is discussed. The injection of fuel takes place at optimal injection timing of $SOI = 310$ °CA BTDC with an injection pressure of 100 bar and constant ignition timing. The parameter settings for this series of experiments are listed in Table 2, last row.

3.3.1 Optical Investigation of In-Cylinder Soot Formation and Oxidation

Soot formation is strongly supported under fuel-rich conditions ($\lambda < 1$) as clearly observable in Figure 17. An

increasing air/fuel ratio results in lower peak soot concentrations. Further, the soot concentration remaining after combustion is strongly reduced by increasing λ and increasing residual oxygen concentration in the subsequent post-oxidation process. The detected signal of the maximum soot concentration from the two-color pyrometry shifts with increasing air/fuel ratio ($\lambda > 1$) to later phases of combustion, despite constant ignition timing. Also, the formation rates of soot decrease reasonably. It should be noted, however, that for the two-color pyrometry the detection volume inside the cylinder is fixed due to the optical arrangement. Consequently, different volumes of the flame inside the cylinder are detected by the two-color optics as the dynamics of the fuel jet and air flow change by varying the air/fuel ratio.

On the one hand, a global lack of oxygen results in fuel-rich and, therefore, incomplete combustion. With increasing

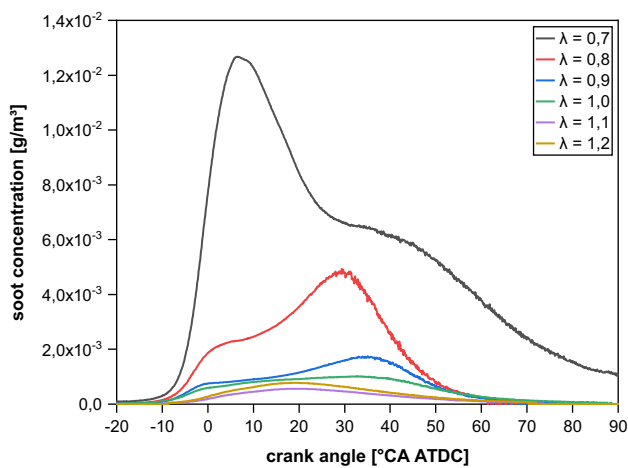


Fig. 17 In-cylinder soot mass concentration for various air/fuel ratios ($n = 2000$ rpm, $BMEP = 8$ bar) determined via two-color pyrometry

air/fuel ratio, the amount of (unburned) fuel that undergoes degradation to hydrocarbon and radical intermediates and, consequently, the concentration of soot precursor molecules such as acetylene is decreasing (compare also Figure 20). Therefore, the growth of aromatic hydrocarbons is no longer favored at high air/fuel ratios resulting in decreasing soot concentration. On the other hand, the oxidation of soot precursors and soot particles, which occurs simultaneously with particle growth, is mainly driven by the availability of oxidative species (O_2 , O , and OH radicals) and flame temperature [43]. While under stoichiometric and especially lean combustion conditions, the soot particles formed are oxidized to a large extent within the post-flame zones, the oxidation of soot is diminished under fuel-rich conditions due to the lack of oxygen and decreasing temperatures and the burnout of soot is shifted to later phases [43].

3.3.2 Exhaust Particle Number Concentration, Particle Size Distributions, and Gaseous Components

The results for exhaust soot particle number concentrations and aggregate size distributions for this set of experiments are presented in Figure 18. Figure 18, lower part, displays an enlarged range of measured size distributions and number concentrations for the air/fuel ratio $0.9 \leq \lambda \leq 1.2$. Particle size distributions are clearly bimodal with a decrease of the particle concentrations of small particles and a shift of the size distributions in the accumulation mode to slightly smaller aggregate sizes with higher air/fuel ratios. The observed variations occur mainly at relative air/fuel ratios ≤ 0.9 . Favorable conditions for an increased particle formation rate are fuel-rich combustion at comparatively low temperatures in the range of 1600 to 1800 K [5]. Changes in oxygen concentration go along with changes in temperature

effecting nonlinearly and via a complex reaction mechanism the formation and oxidation of soot.

TEM images of soot aggregates collected on quartz fiber filters at different relative air/fuel ratios evidence no clear trend of the aggregate sizes with varying air/fuel ratio, see Fig. 19, which is consistent with the results displayed in Fig. 18. However, it has to be noted that the sampling procedure of the aggregates from the exhaust gases possibly influences the appearance of the aggregates.

Soot formation requires high precursor concentrations occurring in global and/or local fuel-rich combustion. Under these conditions, the formation of polyaromatic hydrocarbons (PAH) and primary soot particles is promoted, and their number concentration rises. Increasing particle number concentration inside the cylinder supports the agglomeration of primary particles leading to larger soot aggregates. In turn, stoichiometric and fuel-lean combustion generates low precursor concentrations and consequently to low number concentrations of (primary) particles originally formed during the combustion. Due to the low number concentrations of primary particles, smaller aggregates are formed and a shift of the particle size distributions versus nucleation mode is observed. Excess oxygen at fuel-lean conditions and homogeneous mixtures and, thereby, the enhanced oxidation rate of soot in combination with lower particle number concentrations leads to small aggregates, which then appear also in the exhaust.

In addition to the EEPS data, gaseous emissions and soot mass concentration via filter smoke number (FSN) were measured in the exhaust. As expected, the results displayed in Figure 20 reveal a strong decrease of the measured soot concentration and total concentration of hydrocarbons with increasing air/fuel ratio. The course of measured FSN values with increasing air/fuel ratio is in excellent agreement with that determined via EEPS.

3.3.3 Reactivity of Soot Against Oxidation

Figure 21, left part, shows the normalized TPO profiles of soot samples as a function of the relative air/fuel ratio of the steady-state engine operating points. Fuel-rich operation ($\lambda \leq 0.9$) results in comparably nonreactive particles revealing a reactivity index as low as $RI_{GDI} = 0.12$ (T_{max} of the most prominent fraction x_3 about 618 °C). With increasing air/fuel ratio, RI_{GDI} increases gradually, while T_{max} of the most prominent fractions shift to lower temperatures. At stoichiometric mixture and $\lambda > 1.0$, reactive soot particles with $RI_{GDI} = 0.89$ are formed (T_{max} of the most prominent fraction about 516 °C), indicating a disordered carbon nanostructure and short fringe lengths. This is supported by the kinetic parameters from fitting the TPO profiles applying the three-reactant approach excluding the release of VOC at low temperatures, which is applied also for this series of experiments and RI_{GDI} listed in Table 7. The TPO profiles

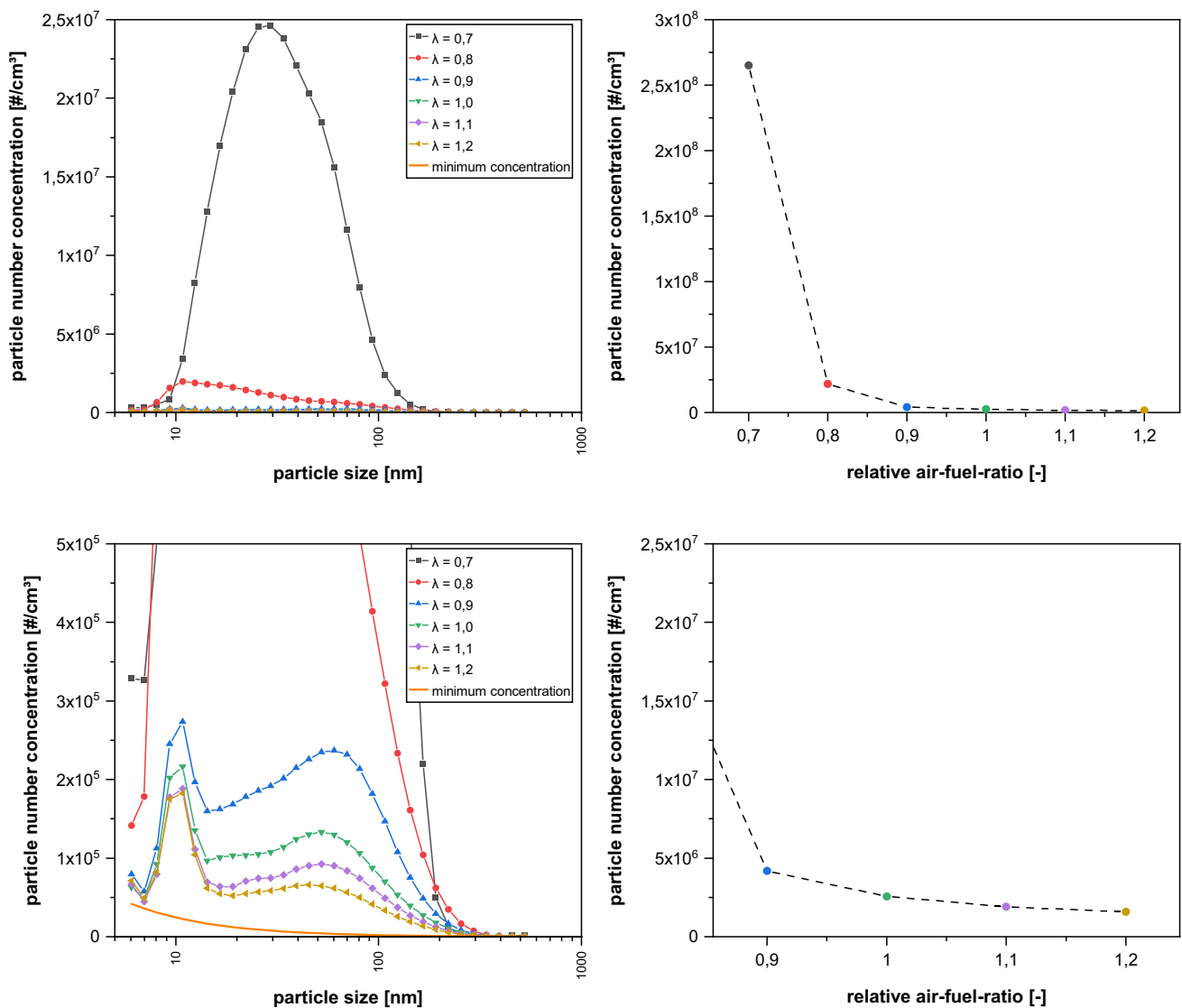


Fig. 18 Upper part: total particle number concentration and mobility size distributions in the exhaust gas at various air/fuel ratios $0.7 \leq \lambda \leq 1.2$ ($n = 2000$ rpm, $BMEP = 8$ bar). Lower part: enlargement for $0.9 \leq \lambda \leq 1.2$; the orange curve represents the detection limit

also evidence the varying formation of the different fractions of nanostructured soot within the soot samples. At $\lambda = 0.7$ and 0.8 , the conversion profiles reveal a proportion of the nonreactive soot particles x_3 of approximately 100 %, while the relative proportions of the reactive fractions are approximately 0 %. In addition, from $\lambda = 0.7$ to $\lambda = 0.8$, $E_{A,3}$ decreases from 141 to 136 kJ/mol, which is also reflected in a decrease of T_{max} of this fraction by 36 °C. With further increase of the relative air/fuel ratio up to stoichiometric and fuel-lean conditions, the TPO profiles exhibit the formation of the more reactive fractions x_2 and x_1 . In addition, the proportion of the nonreactive particles, x_3 , decreases gradually with increasing λ ; see Table 7.

Further increase of the oxygen concentration and lean combustion favors oxidation of initially formed soot in the

post flame zones, generating particles with slightly decreasing extension of fringe layers and, thereby, increasing reactivity.

3.3.4 Carbon Nanostructure and Primary Particle Distribution

Figure 22 displays the results for primary particle size distributions and the carbon nanostructures for the variation of air/fuel ratio. Like in the experiments with engine load ($BMEP$) variations, the CMD , ranging from 21.0 to 28.0 nm, and the geometric standard deviation σ_g ranging from 1.30 to 1.50, do not change systematically as a function of the relative air/fuel ratio (see Figure 22, bottom left). As discussed in Section 3.3.3, RI_{GDI} increases clearly with increasing λ ,

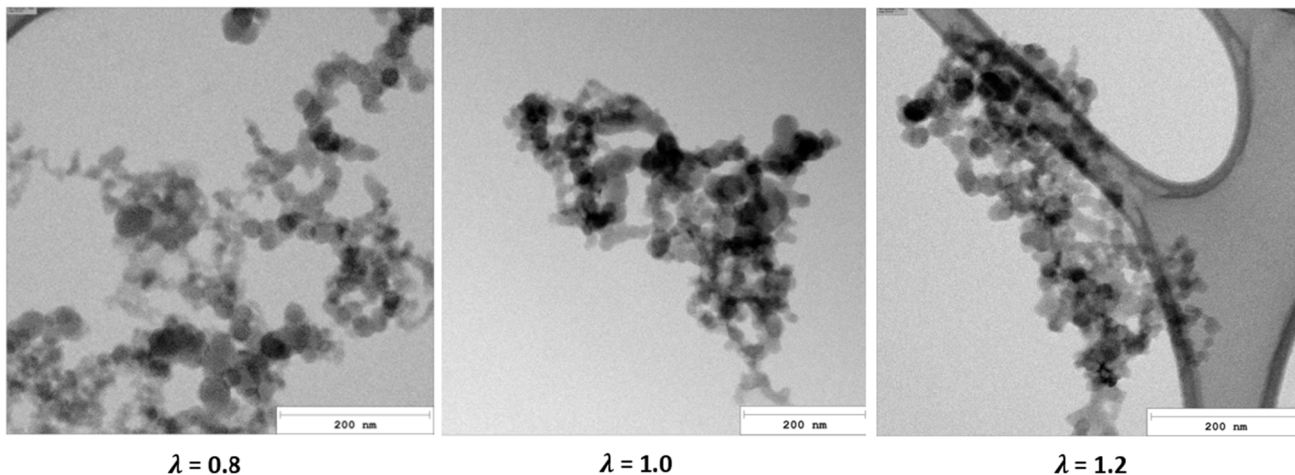


Fig. 19 Soot particle aggregates sampled at various air/fuel ratios at $n=2000$ rpm, $BMEP=8$ bar on quartz fiber filters

Fig. 20 Filter smoke number (FSN) and hydrocarbon concentration for various air/fuel ratios, $n=2000$ rpm, $BMEP=8$ bar

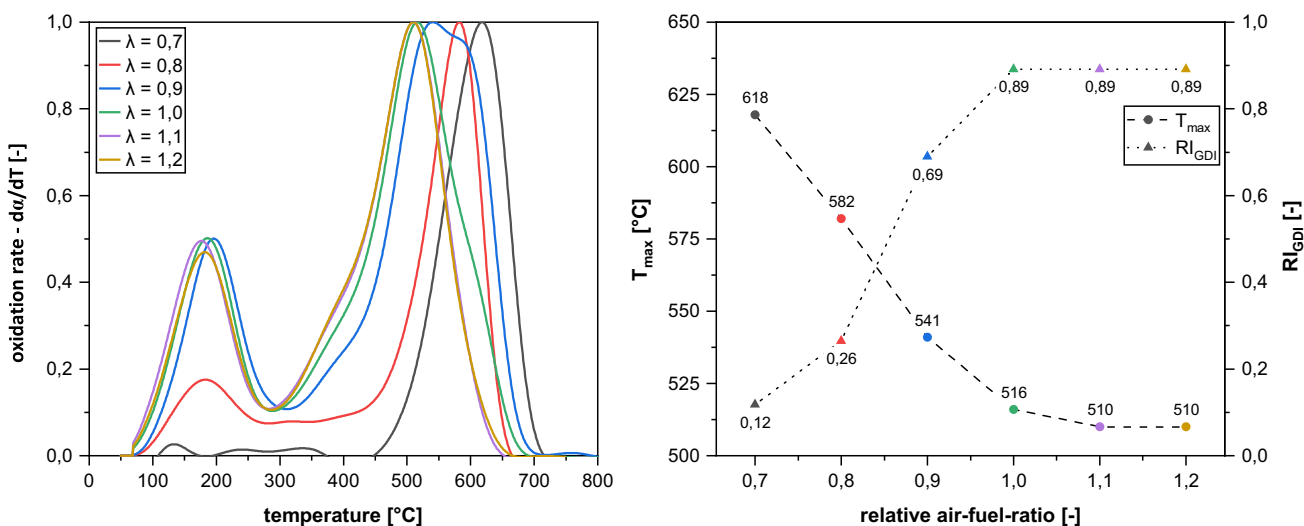
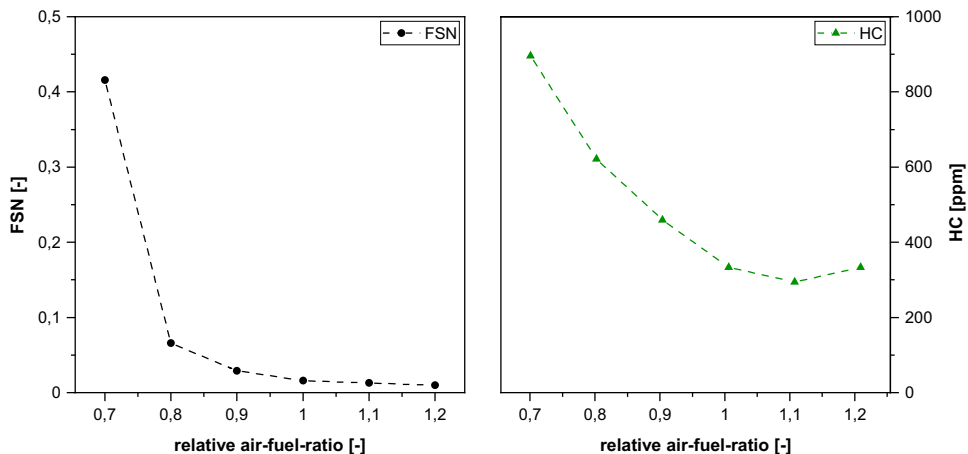


Fig. 21 Experimental oxidation rates $-d\alpha/dT$ of soot samples (left part) and T_{max} for the most prominent fraction of soot as well as reactivity index RI_{GDI} (right part) at various air/fuel ratios, $BMEP=8$ bar, $n=2000$ rpm

Table 7 Kinetic parameter for the oxidation of soot samples from relative air/fuel ratio variations (BMRP = 8 bar, n = 2000 rpm)

λ	x_1 [%]	$k_{0,ox,1}$ [$\text{kg}^{n_{ox,1}-1} \text{K}^{-1}$]	$E_{A,1}$ [kJ/mol]	$n_{ox,1}$ [-]	x_2 [%]	$k_{0,ox,2}$ [$\text{kg}^{n_{ox,2}-1} \text{K}^{-1}$]	$E_{A,2}$ [kJ/mol]	$n_{ox,2}$ [-]	x_3 [%]	$k_{0,ox,3}$ [$\text{kg}^{n_{ox,3}-1} \text{K}^{-1}$]	$E_{A,3}$ [kJ/mol]	$n_{ox,3}$ [-]	RI_{GDI} [-]
0.7	-	-	-	-	-	-	-	-	100	$4 \cdot 10^6$	141	1.0	0.12
0.8	-	-	-	-	-	-	-	-	100	$4 \cdot 10^6$	136	1.0	0.26
0.9	5	$2 \cdot 10^6$	99	1.1	40	$3 \cdot 10^6$	122	1.1	55	$4 \cdot 10^6$	138	1.0	0.69
1.0	8	$2 \cdot 10^6$	94	1.1	54	$3 \cdot 10^6$	121	1.1	38	$4 \cdot 10^6$	136	1.0	0.89
1.1	10	$2 \cdot 10^6$	96	1.1	59	$3 \cdot 10^6$	119.5	1.1	31	$4 \cdot 10^6$	131.5	1.0	0.89
1.2	10	$2 \cdot 10^6$	96	1.1	60	$3 \cdot 10^6$	119.5	1.1	30	$4 \cdot 10^6$	131.5	1.0	0.89

which again indicates that the primary particle size distribution has only a minor effect on soot reactivity regarding oxidation (see Figure 22, bottom right).

In contrary, the carbon nanostructural particle properties change significantly in dependence on the relative air/fuel ratio. $L_{f,mean}$ and $L_{f,90}$ increase gradually with decreasing λ ; see Figure 23. This implies that sub-stoichiometric combustion favors the formation of large graphene-like layers embedded within the primary particles and vice versa. A more advanced oxidation of soot particles causes a reduction of the fringe lengths, as reported in [19]. This is obvious from Figure 23 comparing the fringe length distributions at $\lambda = 0.7$ and $\lambda = 1.2$. These findings are in excellent agreement with the results discussed in Section 3.3.3. Short fringes lead to an increased reactivity against oxidation, which is reflected in an increasing RI_{GDI} .

3.3.5 Similarities and Differences

From the results presented so far, some similarities and differences can be extracted. Increasing rotational engine speed, keeping the remaining operating parameters constant, produces mainly increasing total particle number concentrations while affecting reactivity and kinetics of oxidation to a lesser extent. Reactivity expressed with the help of the reactivity index RI_{GDI} decreases with increasing engine speed and, hence, increasing total particle number concentration. Soot aggregates comprise primary particles of diverse nanostructure documented by graphene-like structures of varying extension and, thereby, fractions of different reactivity. Increasing engine speed shifts the proportion of the different fractions to less reactive ones. Variation of engine load results in similar effects: increasing load leads to increasing particle number concentrations along with decreasing reactivity index RI_{GDI} and increasing proportions of the less reactive fractions of soot aggregates. The mean extension $L_{f,mean}$ of the graphene-like layers embedded within the primary particles correlates approximately linearly with RI_{GDI} , i.e., the larger $L_{f,mean}$ the lower RI_{GDI} . Reducing the air/fuel ratio affects the total particle number concentration to a large extent. Increasing air/fuel ratio leads to strongly decreasing total number concentrations of soot aggregates showing increasing reactivity and decreasing $L_{f,mean}$ of the primary particles.

All observed variations relate to strong changes of the total particle number concentrations or soot volume fractions in the exhaust; see Figs. 7, 12, and 18. Figure 24 depicts correlations of the reactivity index RI_{GDI} , the mean fringe length distributions $L_{f,mean}$, the count medium diameter CMD , and the temperature at maximum conversion rate T_{max} of the most prominent fraction with the total number concentration for all the test runs discussed in Sections 3.1 to 3.3. The total particle number concentration is the parameter

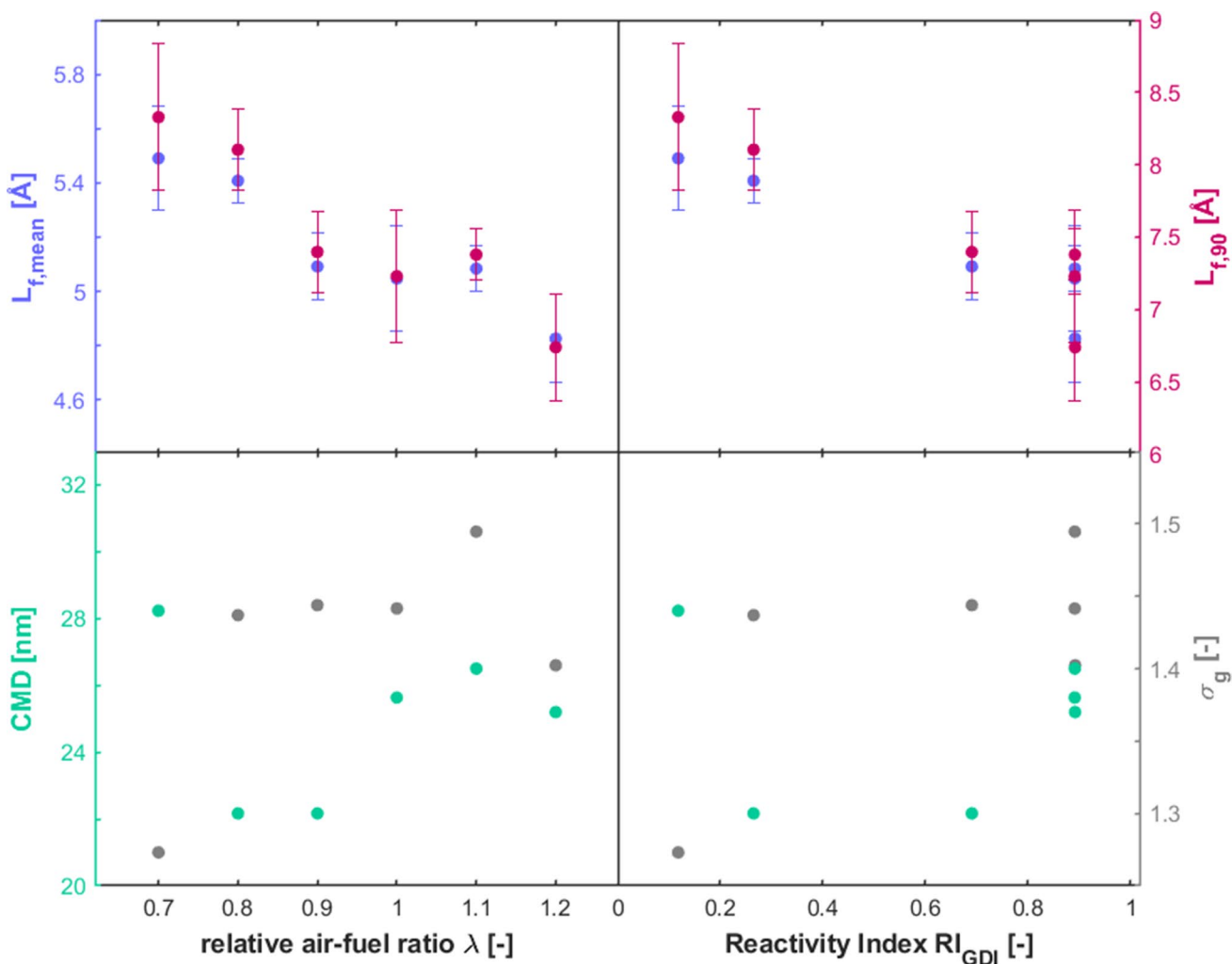


Fig. 22 Mean fringe length (blue symbols) and decile of the fringe length distributions (red symbols), upper part, as well as count median diameter (CMD, green symbols) and geometric standard

deviation of primary soot particle size distributions (grey symbols), lower part, plotted versus air/fuel ratio (left) and RI_{GDI} (right), $BMEP=8$ bar, $n=2000$ rpm

with the strongest changes in the test runs. The CMD of the analyzed primary particle size distributions for all operating points exhibit a poor correlation with the total particle number density (Pearson correlation coefficient $r = -0.36$),

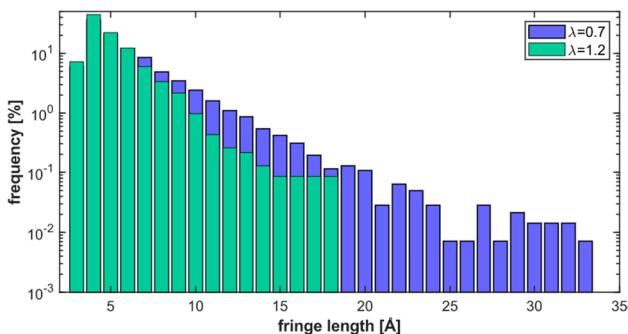
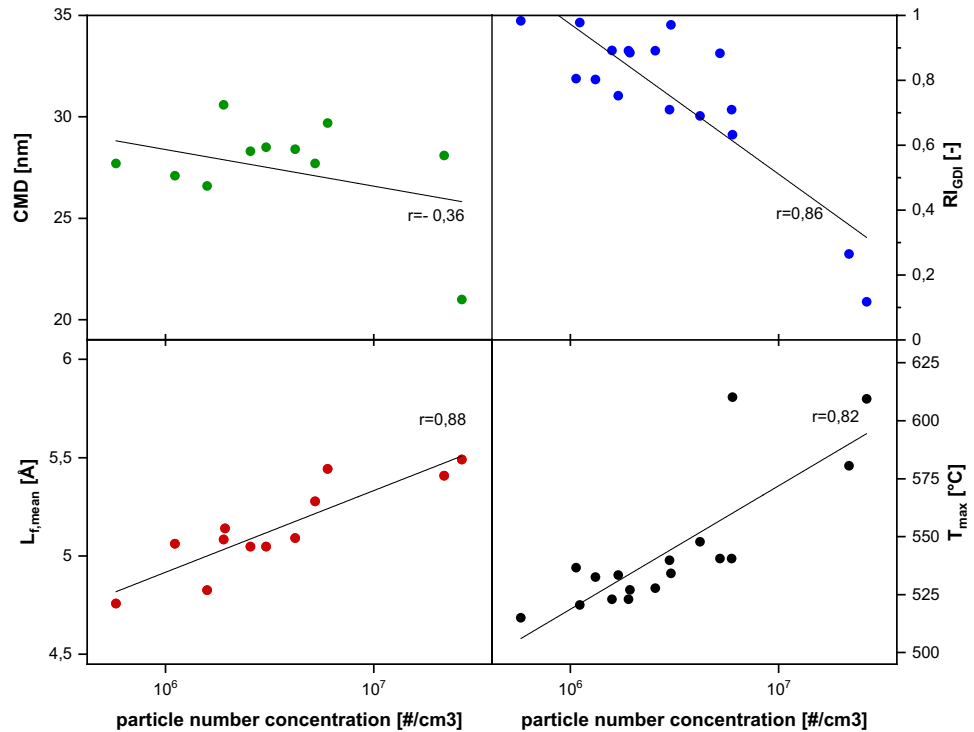


Fig. 23 Comparison of the fringe length distributions of soot particles generated at $\lambda=0.7$ and $\lambda=1.2$ ($BMEP=8$ bar, $n=2000$ rpm)

whereas RI_{GDI} and $L_{f,mean}$ correlate much better ($r = -0.86$ and 0.82 , respectively). As reported in (40) and demonstrated in Fig. 16, RI_{GDI} and $L_{f,mean}$ are well correlated. Therefore, if RI_{GDI} exhibits a good correlation with the total particle number concentration, an equally well correlation of $L_{f,mean}$ should be obvious. The same holds for the correlation of T_{max} and RI_{GDI} . The dependence on total particle number concentration is confirmed by the FSN (see Figs. 14 and 20). Operating points at high engine speed, high engine load, and low relative air/fuel ratio produce high particle number densities and high amounts of soot (large FSN). Soot aggregates appearing under these conditions contain diverse fractions of primary particles with largest proportions of fractions with low reactivity within the soot particles. Decreasing reactivity of the soot particles goes along with increasing extension of graphene-like layers being observed at growing total particle number concentrations and vice versa.

Fig. 24 Correlations of count medium diameter (*CMD*) of primary particle size distributions (top left), mean fringe length $L_{f,mean}$ (bottom left), reactivity index RI_{GDI} (top right), and T_{max} of the most prominent fraction of soot (bottom right) with total particle number concentration measured via EEPs for all operating points examined in this work



The causes for high total particle number concentrations are on the one hand global fuel-rich conditions at constant engine speed and load and, on the other hand, high rotational engine speed and high load at overall stoichiometric conditions. As discussed in Sections 3.1 and 3.2, increasing engine speed and enlarging engine load is accompanied by growing formation of mixture inhomogeneities with fluid parcels of varying mixture composition. Combustion inside the cylinder includes the different fluid parcels, forming soot in sufficiently fuel-rich fluid parcels. The properties of soot formed depends on the local mixture composition and increasingly fuel-rich conditions lead to growing total particle concentrations with primary particles of increasing extension of the graphene-like layers. Primary particles being formed within fluid parcels of different composition, and, therefore, different nanostructural properties retain these when accumulated to larger aggregates. During the post flame zone oxidation most of the soot is oxidized, however, soot particles surviving oxidation reflect their combustion history and conserve their nanostructural properties to a large extent when appearing in the exhaust. These different nanostructural properties turn out, e.g., in the TPO experiments. Changes of global mixture composition at constant moderate engine speed and load are characterized by more homogeneous mixture composition. Under conditions of < 1.0 , due to the increasing amount of fuel injected, inhomogeneities in the formation of the fuel/air mixture may occur, and the least reactive soot fraction dominates. At λ

> 1.0 , soot particles with high reactivity and small sizes of graphene-like structures at low total particle number concentrations are formed.

4 Summary and Conclusions

The main objective of this study is the investigation of the effect of the global engine operating parameters, viz., engine speed, brake mean effective pressure, and relative air/fuel ratio of a turbocharged 4-cylinder direct injection gasoline engine on reactivity of emitted soot against oxidation. Knowledge of this parameters is crucial for the design of Gasoline Particulate Filters (GPF) and their regeneration strategies. Reactivity against oxidation by molecular oxygen was determined ex situ via temperature programmed oxidation (TPO) of soot samples collected during stationary operating points. Both, the reactivity index RI_{GDI} , which takes into account the reaction rate at defined conditions, as well as the temperature of maximum oxidation rate, T_{max} , were used to characterize soot reactivity.

The obtained results reveal that engine operating parameters and conditions affect soot reactivity differently. While engine speed has only slight effect, a reduction of the relative air/fuel ratio or an increase in engine load (*BMEP*) significantly reduce the soot reactivity. While reactive soot particle aggregates generated at $\lambda \geq 1.0$ and $BMEP \leq 8$ bar

are composed of multiple soot fractions of different reactivity and activation energies, conversion profiles at $\lambda < 1.0$ and $BMEP > 10$ bar show a single peak corresponding to a nonreactive soot fraction with $E_{A,3} > 136$ kJ/mol. Based on these findings, the quality of mixture formation, the degree of inhomogeneities in the gas phase, and, therefore, the combustion mode (process) presumably are significant parameters influencing soot reactivity. The closer the combustion mode of the investigated GDI engine approaches premixed combustion with homogeneous fuel/air mixture field, the more reactive the emitted soot particles. This hypothesis also accounts for the minor differences in T_{max} and RI_{GDI} analyzed for the engine speed variation.

Reactivity of soot particles partly varies strongly among the examined operating points. To link reactivity to in-cylinder combustion, soot concentrations were determined both in-cylinder and in the exhaust gas. The time-resolved soot concentrations determined within the cylinder show that high-reactivity particles are connected with operating points forming small amounts of soot. In-cylinder soot post-oxidation at high temperatures and oxygen concentrations reduces concentration of initially formed soot. In the exhaust gas, therefore, comparatively small number concentrations and mass fractions are detected via EEPS and smoke meter. The results substantiate the hypothesis that non-sooty largely premixed combustion of a homogeneous fuel/air mixture field not only suppresses soot formation but also favors formation of reactive soot fractions. Therefore, the results of the study support the conclusions derived from [14, 30], and [31] linking increasing inhomogeneities of the fuel/air mixture field with decreasing soot reactivity.

Soot reactivity against oxidation can be controlled by the examined global operating parameters. This knowledge is important to ensure little effort GPF regeneration. Soot particle aggregates consisting predominantly of reactive particles with short graphene-like layers are emitted whenever an optimal homogeneous fuel/air mixture field with $\lambda \geq 1$ is provided, resulting simultaneously in a low particle number and mass concentration.

Acknowledgements The authors are very grateful to the German Research Foundation (DFG) for funding this research as part of the projects TR470/7-2, KO4830/2-2, and SU249/6-2. Moreover, the authors would like to thank Prof. Dagmar Gerthsen and Dr. Heike Störmer from the Laboratory for Electron Microscopy at Karlsruhe Institute of Technology (KIT) for their very valuable help with the HRTEM experiments.

Funding Open Access funding enabled and organized by Projekt DEAL.

Declarations

Conflict of Interest The authors declare no competing interests.

Open Access This article is licensed under a Creative Commons Attribution 4.0 International License, which permits use, sharing, adaptation, distribution and reproduction in any medium or format, as long as you give appropriate credit to the original author(s) and the source, provide a link to the Creative Commons licence, and indicate if changes were made. The images or other third party material in this article are included in the article's Creative Commons licence, unless indicated otherwise in a credit line to the material. If material is not included in the article's Creative Commons licence and your intended use is not permitted by statutory regulation or exceeds the permitted use, you will need to obtain permission directly from the copyright holder. To view a copy of this licence, visit <http://creativecommons.org/licenses/by/4.0/>.

References

- Saliba, G., Saleh, R., Zhao, Y., et al.: Comparison of gasoline direct-injection (GDI) and port fuel injection (PFI) vehicle emissions: emission certification standards, cold-start, secondary organic aerosol formation potential, and potential climate impacts. *Environ. Sci. Technol.* **51**, 6542–6552 (2017). <https://doi.org/10.1021/acs.est.6b06509>
- Su, D., Serafino, A., Müller, J.-O., Jentoft, R., Schlögl, R., Fiorito, S.: Cytotoxicity and inflammatory potential of soot particles of Low-emission diesel engines. *Environ. Sci. Technol.* **42**, 1761–1765 (2008)
- Commission Regulation (EU) No. 459/2012 (2012)
- Mansurov, Z.A.: Soot formation in combustion Processes. *Combustion, Explosion and shock waves* **41**, 727–744 (2005). <https://doi.org/10.1007/s10573-005-0083-2>
- Steimle, F., Kulzer, A., Richter, H., et al.: Systematic analysis and particle emission reduction of homogeneous direct injection SI engines. SAE Technical Paper. 2013–01–0248 (2013). <https://doi.org/10.4271/2013-01-0248>
- Velji, A., Yeom, K., Wagner, U., et al.: Investigations of the formation and oxidation of soot inside a direct injection spark ignition engine using advanced laser-techniques. SAE Technical Paper. 2010–01–0392 (2010). <https://doi.org/10.4271/2010-01-0352>
- Dageförde, H., Bertsch, M., Kubach, H., et al.: Reduktion der Partikelemission bei Ottomotoren mit Direkteinspritzung. *Motortechnische Zeitschrift* **76**, 86–93 (2015). <https://doi.org/10.1007/s35146-015-0108-7>
- Sharma, N., Agarwal, A.: Gasoline direct injection engines and particulate emissions. *Air. Pollut. Control.*, 87–105 (2017). https://doi.org/10.1007/978-981-10-7185-0_6
- Potenza, M., Milanese, M., de Risi, A.: Effect of injection strategies on particulate matter structures of a turbocharged GDI engine. *Fuel* **237**, 413–428 (2019). <https://doi.org/10.1016/j.fuel.2018.09.130>
- Jiang, C., Xu, H., Srivastava, D., et al.: Effect of fuel injector deposit on spray characteristics, gaseous emissions and particulate matter in a gasoline direct engine. *Appl. Energy*. **203**, 390–402 (2017). <https://doi.org/10.1016/j.apenergy.2017.06.020>
- Easter, J.E., Fiano, A., Bohac, S., et al.: Evaluation of low mileage GPF filtration and regeneration as influenced by soot morphology, reactivity, and GPF loading. SAE Technical Paper. 2019–01–0975 (2019). <https://doi.org/10.4271/2019-01-0975>
- Fiebig, M., Schönen, M., Grütering, U., et al.: Einflüsse motorischer Betriebsparameter auf die Reaktivität von Dieseleruss. *Motortechnische Zeitschrift* **71**, 524–531 (2010). <https://doi.org/10.1007/BF03225593>
- Niessner, R.: The Many Faces of Soot: Characterization of soot nanoparticles produced by engines. *Angew. Chem.* **53**, 12366–12379 (2014). <https://doi.org/10.1002/anie.201402812>

14. Seong, H., Lee, K., Choi, S.: Effects of engine operating parameters on morphology of particulates from a gasoline direct injection (GDI) engine. SAE Technical Paper. 2013–01–2574 (2013). <https://doi.org/10.4271/2013-01-2574>
15. Uy, D., Monica, A. Ford., Douglas, Jayne., et al.: Characterization of gasoline soot and comparison to diesel soot: Morphology, chemistry, and wear. *Tribol. Int.* **80**, 198–209 (2014). <https://doi.org/10.1016/j.triboint.2014.06.009>
16. Lee, K.O., Cole, R., Sekar, R., et al.: Morphological investigation of the microstructure, dimensions, and fractal geometry of diesel particulates. *Proc. Combust. Inst.* **29**, 647–653 (2002). [https://doi.org/10.1016/S1540-7489\(02\)80083-9](https://doi.org/10.1016/S1540-7489(02)80083-9)
17. Gaddam, C.K., Vander Wal, R.L.: Physical & chemical characterization of SIDI engine particulates. *Combust. Flame.* **160**, 2517–2528 (2012). <https://doi.org/10.1016/j.combustflame.2013.05.025>
18. Luo, Y., Thu, L., Fang, J., et al.: Size distribution, chemical composition and oxidation reactivity of particulate matter from gasoline direct injection (GDI) engine fueled with ethanol-gasoline fuel. *Appl. Therm. Eng.* **89**, 647–655 (2015). <https://doi.org/10.1016/j.applthermaleng.2015.06.060>
19. Hagen, F.P., Hardock, F., Koch, S., et al.: Why soot is not alike soot: a molecular/nanostructural approach to soot oxidation on particulate filters. *Flow, turbulence and combustion* **106**, 295–329 (2020). <https://doi.org/10.1007/s10494-020-00205-2>
20. Vander Wal, R., Tomasek, A.: Soot oxidation: dependence upon initial nanostructure. *Combust. Flame.* **134**, 1–9 (2003). [https://doi.org/10.1016/S0010-2180\(03\)00084-1](https://doi.org/10.1016/S0010-2180(03)00084-1)
21. Smith, D.M., Chughtai, A.R.: The surface structure and reactivity of black carbon. *Colloids Surf., A* **105**, 47–77 (1995). [https://doi.org/10.1016/0927-7757\(95\)03337-1](https://doi.org/10.1016/0927-7757(95)03337-1)
22. Lu, T., Cheung, C.S., Huang, Z.: Size-resolved volatility, morphology, nanostructure, and oxidation characteristics of diesel particulate. *Energy Fuels* **26**, 6168–6176 (2012). <https://doi.org/10.1021/ef3010527>
23. Fang, H., Lance, M.: Influence of soot surface changes on DPF regeneration. SAE International. 2004–01–3043 (2004). <http://www.jstor.org/stable/44740913>.
24. Aarna, I., Suuberg, E.: A review of the kinetics of the nitric oxide-carbon reaction. *Fuel* **76**, 475–491 (1997). [https://doi.org/10.1016/S0016-2361\(96\)00212-8](https://doi.org/10.1016/S0016-2361(96)00212-8)
25. Rinkenburger, A., Toriyama, T., Yasuda, K., et al.: Catalytic effect of potassium compounds in soot oxidation. *Chem. Cat. Chem.* **9**, 3513–3525 (2017). <https://doi.org/10.1002/cctc.201700338>
26. Su, D.S., Müller, J.-O., Jentoft, R.E., et al.: Fullerene-like soot from EuroIV diesel engine: consequences for catalytic automotive pollution control. *Top. Catal.* **30**, 241–245 (2004). <https://doi.org/10.1023/B:TOCA.0000029756.50941.02>
27. Su, D.S., Jentoft, R.E., Müller, J.-O., et al.: Microstructure and oxidation behaviour of Euro IV diesel engine soot: a comparative study with synthetic model soot substances. *Catal. Today.* **90**, 127–132 (2004). <https://doi.org/10.1016/j.cattod.2004.04.017>
28. Song, J., C., Song, Tao Y., Lv G., et al.: Diesel soot oxidation during the late combustion phase. *Combustion and Flame* **158**, 446–451 (2011). <https://doi.org/10.1016/j.combustflame.2010.09.017>
29. Zygogianni, A., Syrigou, M., Konstandopoulos, A., et al.: Oxidative reactivity of particulate samples from different diesel combustion systems and its relation to structural and spectral characteristics of soot. *Emission. Cont. Sci. Technol.* **5**, 99–123 (2019). <https://doi.org/10.1007/s40825-019-00118-1>
30. Koch, S., Hagen, F. P., Kubach, H., et al.: Impact of the injection strategy on soot reactivity and particle properties of a GDI engine. SAE Technical Paper. 2020–01–0392 (2020). <https://doi.org/10.4271/2020-01-0392>
31. Miyasjita, K., Fukufa, Y., Shiozaki, Y., et al.: TEM analysis of soot particles sampled from gasoline direction injection engine exhaust at different fuel. SAE Technical Paper. 2015–01–1872 (2015). <https://doi.org/10.4271/2015-01-1872>
32. Choi, S., Seong, H.: Oxidation characteristics of gasoline direct-injection (GDI) engine soot: catalytic effects of Ash and modified kinetic correlation. *Combust. Flame.* **162**, 2371–2389 (2015). <https://doi.org/10.1016/j.combustflame.2015.02.004>
33. Jiang, L., Gu, C., Huo, J., et al.: Improved two-color method for temperature measurement of soot flames. *Journal of Thermophysics and Heat Transfer* **0**, 1–9 (2021). <https://doi.org/10.2514/1.T6395>
34. Schubiger, R.A., Boulouchous, K., Ebberle, M.: Rußbildung und Oxidation bei der dieselmotorischen Verbrennung. *MTZ* **63**, 342–353 (2002). <https://doi.org/10.1007/BF03227355>
35. Epp, M., Niendorf, M., Hassel, E., et al.: Drei-Farben spektrometrische Temperaturbestimmung mit einer CMOS-Hochgeschwindigkeitskamera am Einzylinder-Forschungsmotor. Fachtagung “Lasermethoden in der Strömungsmesstechnik” (2012)
36. Stumpf, M., Velji, A., Spicher, U., et al.: Investigations on soot emission behavior of a common-rail diesel engine during steady and non-steady operating conditions by means of several measuring techniques. SAE Technical Paper. 2005–01–2154 (2005). <https://doi.org/10.4271/2005-01-2154>
37. Hagen, F.P., Rinkenburger, A., Günther, J., et al.: Spark discharge-generated soot: Varying nanostructure and reactivity against oxidation with molecular oxygen by synthesis conditions. *J. Aerosol Sci.* **143**, 105530 (2020). <https://doi.org/10.1016/j.jaerosci.2020.105530>
38. Bogorra, M., Herreros, J.M., Tsolakis, A., et al.: Gasoline direct injection engine soot oxidation: fundamentals and determination of kinetic parameters. *Combust. Flame* **190**, 177–187 (2018). <https://doi.org/10.1016/j.combustflame.2017.11.027>
39. Muller, P.: Glossary of terms used in physical organic chemistry. *Pure Appl. Chem.* **66**, 1077–1184 (1994). <https://doi.org/10.1351/pac199466051077>
40. Hagen, F.P., Kretzler, D., Häber, T., et al.: Carbon nanostructure and reactivity of soot particles from non-intrusive methods based on UV-VIS spectroscopy and time-resolved laser-induced incandescence. *Carbon* **182**, 634–654 (2021). <https://doi.org/10.1016/j.carbon.2021.06.006>
41. Hagen, F.P., Bockhorn, H., Störmer, H., et al.: Nanostructural and morphological characteristics of single soot aggregates during low-temperature oxidation. *Proceedings of the Combustion Institute* **38**, 1153–1161 (2020). <https://doi.org/10.1016/j.proci.2020.06.338>
42. K. Yehliu, K. Vander Wal, R.L., Boehman, A.L.: Development of an HRTEM image analysis method to quantify carbon nanostructure. *Combust. Flame* **158**, 1837–1851 (2011). <https://doi.org/10.1016/j.combustflame.2011.01.009>
43. Zhang, T.Y., Suen, C.Y.: A fast parallel algorithm for thinning digital patterns, *communications of the ACM* **27**, 236–239 (1984). <https://doi.org/10.1145/357994.358023>
44. Appel, J., Bockhorn, H., Frenklach, M.: Kinetic modeling of soot formation with detailed chemistry and physics. *Combust. Flame* **121**, 122–136 (2000). [https://doi.org/10.1016/S0010-2180\(99\)00135-2](https://doi.org/10.1016/S0010-2180(99)00135-2)
45. Neoh, K.G., Howard, J.B., Sarofim, A.F.: Effect of oxidation on physical structure of soot. Twentieth Symposium (International) on Combustion **20**, 951–957 (1984). [https://doi.org/10.1016/S0082-0784\(85\)80584-1](https://doi.org/10.1016/S0082-0784(85)80584-1)